8-2006

Ultraviolet Image Analysis of Spacecraft Exhaust Plumes

Karen L. Norton
University of Tennessee - Knoxville

To the Graduate Council:

I am submitting herewith a thesis written by Karen L. Norton entitled "Ultraviolet Image Analysis of Spacecraft Exhaust Plumes." I have examined the final electronic copy of this thesis for form and content and recommend that it be accepted in partial fulfillment of the requirements for the degree of Master of Science, with a major in Physics.

Lloyd M. Davis, Major Professor

We have read this thesis and recommend its acceptance:

Horace W. Carter, Christian G. Parigger

Accepted for the Council:
Dixie L. Thompson

Vice Provost and Dean of the Graduate School

(Original signatures are on file with official student records.)

To the Graduate Council:

I am submitting herewith a thesis written by Karen L. Norton entitled "Ultraviolet Image Analysis of Spacecraft Exhaust Plumes." I have examined the final electronic copy of this thesis for form and content and recommend that it be accepted in partial fulfillment of the requirements for the degree of Master of Science with a major in Physics.

Lloyd M. Davis
_____
Major Professor

We have read this thesis
and recommend its acceptance:

Horace W. Crater
_____

Christian G. Parigger
_____

Accepted for the Council:

Anne Mayhew
_____
Vice Chancellor and
Dean of Graduate Studies

(Original signatures are on file with official student records.)

ULTRAVIOLET IMAGE ANALYSIS OF SPACECRAFT EXHAUST PLUMES

A Thesis

Presented for the

Master of Science

Degree

The University of Tennessee, Knoxville

Karen L. Norton

August 2006

Dedication

This thesis is dedicated to Mr. Vance Merritt, Bangor High School's physics teacher extraordinaire. Mr. Merritt's enthusiasm for the sciences was conveyed to his students daily with wit and wisdom. He demonstrated unfailing confidence in every class member's ability to grasp the intricacies of the physical sciences. So it was that 18 years after leaving his classroom, I was able to take up his torch and seek out the physics challenge.

Acknowledgement

My sincerest thanks go to the Missile Defense Agency for financing this project through their *Legacy* program.

The technical expertise and experience of the talented people at the Advanced Missile Signature Center at Arnold Engineering and Development Center has been immeasurable. Specifically, Dr. Wheeler McGregor has allowed me access to his wealth of knowledge on the topic of plumes. My deepest thanks go to Dr. Bob Reed for his tutoring in Matlab and star calibration techniques. Additionally, Clare Zisk conducted valuable training on Unix-based tools and often provided the push that kept me moving forward. My thanks also to Dr. William Dimpfl of Aerospace Corporation and Dr. Deborah Levin of Pennsylvania State University for their accessibility and patience in explaining the finer points of their respective published material.

No 'Thank you' would be complete without noting the staff and faculty of the University of Tennessee Space Institute. The support and genuine caring exhibited by this team make the facility more than just an institute of higher learning; they make it a family. Specifically, I would like to notice Linda Engel for her direction in the layout of this thesis, and Dr. Pavlina Pike for her proof-reading. My thanks also to my Thesis Advisory Committee, consisting of Dr. Lloyd Davis, Dr. Horace Crater, and Dr. Christian Parigger, for their guidance and motivation.

Finally, I would like to recognize the support, tolerance and understanding of my family as I set out on this task. Success is never quite so sweet as when we share it with those we love.

Abstract

Data obtained during the April 26, 2000 *MirEx* experiment is used to infer the chemical mechanisms responsible for ultraviolet radiation observed to emanate from Russian spacecraft exhaust plumes in low Earth orbit. The principle objective of this experiment was to use the *Mir* Space Station instruments to study the plume collisional processes occurring in the rarified atmosphere of the far-field; at distances greater than one kilometer away from the spacecraft. This was accomplished by observing the automated *Progress* cargo ship as the auxiliary engines were being retrofired in a ram-burn configuration at 330 kilometers in altitude above Earth. The primary emitters, observed within the 240 nm to 360 nm operating region of the instruments, were the molecular transitions of OH ($A\ ^2\Sigma^+ \rightarrow X\ ^2\Pi$), occurring at 306 nm, and NH ($A\ ^3\Pi \rightarrow X\ ^3\Sigma^-$), occurring at 336 nm.

Proposed reactions for forming the excited-state OH and NH molecules begin with the ambient gases present in the upper thermosphere. The collision pair for the atmospheric species is postulated to be gaseous water, which is expelled as a product of rocket engine combustion. It is concluded that the most likely atmospheric species are atomic oxygen and nitrogen. The activation energy for both reactions is the same; that energy required to break an O-H bond in the water. The inclusion of the atmospheric wind velocity contribution to the collision velocity is proven to provide sufficient energy for each of the proposed reactions to proceed.

Contents

List of Tables

List of Figures

List of Acronyms

Acronym	Term
ACS	Attitude Control System
AEDC	Arnold Engineering Development Center
AFRL	Air Force Research Laboratory
AIAA	American Institute of Aeronautics and Astronautics
AMSC	Advanced Missile Signature Center
ASCII	American Standard Code for Information Interchange
CCD	Charge Coupled Device
DSMC	Direct Simulated Monte Carlo
EOARD	European Office of Aerospace Research and Development
FOV	Field of View
FFT	Fast Fourier Transform
GUI	Graphical User Interface
IR	Infrared
ISTC	International Science and Technology Center
ITEA	International Technology Education Association
LEO	Low Earth Orbit
MSIS	Mass-Spectrometer-Incoherent-Scatter
NARJ	Numerical Analysis of Real Jets
NIR	Near Infrared
PAL	Phase Alternating Line
PME	Progress Main Engine
S&T	Science and Technology
SAF	Standard Archive Format
T&E	Test and Evaluation
TsN	Central Research Institute for Machine Building
TsNIIMASH	Central Research Institute for Machine Building
UDMH	Unsymmetric Dimethylhydrazine
US	United States
UT	Universal Time
UV	Ultraviolet
VUV	Vacuum Ultraviolet

1 Introduction

In 1994, the Russian Space Agency publicly released ultraviolet imagery of the plume emissions of a shuttle spacecraft retro-firing in the vicinity of the *Mir* Space Station. Dialogs ensued between scientists at the Central Research Institute for Machine Building, or TsNIIMASH (TsN),[1] the Russian center for aerospace thermodynamics and space mission analysis, and Arnold Engineering Development Center (AEDC), an American aerospace simulation, testing, and evaluation center. Collaboration, in conjunction with the United States Air Force Research Laboratory (AFRL), was proposed to conduct scientific space experiments using the research equipment readily available onboard *Mir*.

A comprehensive examination of the *Mir* Space Station, its service spacecraft, and the program to study the exhaust plumes of those spacecraft is presented in Chapter 1. Chapter 2 outlines the operating environment of the spacecraft and the observation scenario for this experiment. Chapter 3 describes the instrumentation available on *Mir* for observation of plumes. Chapter 4 examines the spectroscopic data while Chapter 5 examines the imagery data generated on April 26, 2000. Chapter 6 presents several chemical mechanisms as sources for the spectral and image data collected. Finally, Chapter 7 discusses the viability of the proposed mechanisms and offers ideas for continuing research using this data set.

In this first chapter, an overview of the United States (US) sponsored program for experimentation onboard the *Mir* Space Station is given. Section 1.1 presents a brief history of the Russian Space Station. In Section 1.2, initiation of a joint effort between the US and Russia for experimentation in low Earth orbit is explained. Section 1.3 describes the Russian spacecraft used to both service the Space Station and as the objects of observation for this experiment. Section 1.4 summarizes the conclusion of this collaborative effort.

1.1 Mir

On March 15, 1986 the *Mir* Space Station began manned operations. *Mir*, or Мир in Russian, was designed by the S. P. Korolev Rocket & Space Corporation *Energia,* and modularly developed with the participation of over 200 Soviet organizations.[2] It replaced the Salyut space stations, a series of orbital modules which were operated throughout the 1970s and 1980s by the Soviets. The station's C*ore* module was launched by the *Proton* launch vehicle at an inclination of 51.6 degrees on February 20, 1986. This inclination avoided flying through Chinese air-space to deposit the module into low Earth orbit (LEO). Five orbital components followed; which, when docked with the *Core*, comprised the *Mir* Space Station, which is depicted in figure 1.

The C*ore* module, which measured 15 x 4.15 meters, was the living quarters for the cosmonauts. Weighing 20,000 kilograms (kg), it provided the life support, power generation and thermal control for the completed station.[3] Launched on March 31, 1987, Квант, or *Kvant* in English, was the astrophysical research module. Weighing 11,000 kg, *Kvant* contained the Roentgen astrophysics observatory, along with Pulsar x-ray telescopes, a gamma ray detector and the Glazar UV telescope. Measuring 5.8 x 4.15 meters, this module also had the 14 meter long Sofora mast structure mounted to its exterior. The 20,000 kg *Kvant-2* was launched on November 26, 1989. It contained the crew shower facility and the airlock used by Cosmonauts for extra-vehicular activities, and measured 12 x 4.4 meters.

The next *Mir* module, Кристалл, or *Krystall*, was launched on May 31, 1990. At 12 x 4.4 meters, it housed the Earth observation instruments and was used to develop biological and semiconductor material technologies in space. It was followed on May 20, 1995 by the 19,640 kg Спектр, or *Spektr,* the remote sensing geophysical research module. Measuring 12 x 4.35 meters, *Spektr* included the externally mounted apparatus for experiments outside of *Mir*. The 19,700 kg remote sensing module Природа, or *Priroda,* was launched on April 23, 1996. This 12 x 4.35 meter module contained a synthetic aperture

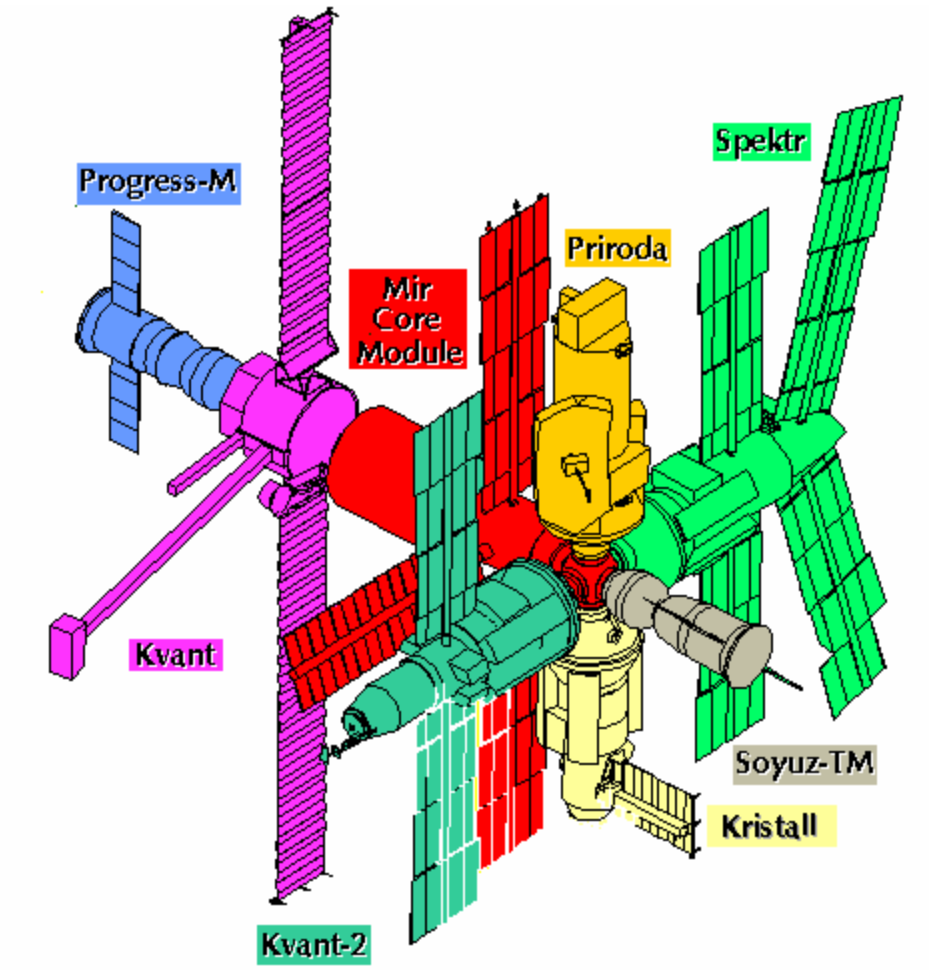

Figure 1. Modules of the Mir Space Station.

radar, active and passive radiometers, and optical scanners. *Priroda* also carried visible and infrared spectrometers for measuring atmospheric concentrations of aerosols and ozone. When completed, the *Mir* Space Station measured 27 meters high, 32 meters long, and 30 meters wide.

The mission of the Space Station was scientific and applied research, over an expected operational lifetime of five years. *Mir* was replenished by two models of service vehicles; the manned transport Союз, or *Soyuz,* provided crew rotations and the automated Прогресс, or *Progress*, provided cargo transport. With a permanent crew and reliable logistical support, *Mir* provided an unmatched opportunity to conduct observations of Earth and its neighbors, as well as studies of basic physical phenomenon in space. Fifty five scientific programs, of both Russian and international origin, were fulfilled utilizing *Mir*.

1.2 MirEx

Ultraviolet (UV) and infrared (IR) glow had been previously observed emanating from US shuttle craft.[4,5] The source of this glow was postulated to be collisions of monatomic oxygen in the Earth's upper atmosphere with the effluent plume molecules. In-situ radiometric measurements were taken on the shuttle itself, of its own engines. This provided data in the near-field region; that region within meters of the engines, where the exhaust gases freely expand into space. However, no information about the extended profile of the plume, in the far-field region where the expanding exhaust gases interact with the ambient atmosphere, was gathered. By using *Mir* as the observation platform, valuable information about exhaust plumes in the far-field, many kilometers away from the spacecraft, would be gathered.

In 1997, a joint scientific program began that was named in Russia *Relaxation,* to study the physical process responsible for radiation. The United States collaboration with this program was called *MirEx*. This program had four primary goals: the studies of atmospheric science, re-entry physics, electric propulsion systems and atmosphere-plume interaction. The fourth goal

resulted in the research of which this research is a small part. This project was designed to investigate spacecraft rocket exhaust plumes and their radiative behavior in the space. With funding provided by the US Air Force Office of Scientific Research and planning completed by AEDC and AFRL, three years of experimentation began.

Far-field plume UV images observed by *Mir* during the initial 1997 *MirEx* experiment could not be adequately described by existing kinetic equation solutions. Therefore, plume spectral radiation equipment supplied by the US was transported to *Mir*. The Russian cosmonauts collected data from *Soyuz-TM* and *Progress-M* spacecraft plumes as the replenishment vehicles arrived and departed from the Space Station. These initial opportunistic collections of exhaust plume data led to dedicated spacecraft maneuvers designed to gather valuable data which could provide insight into modeling of the chemical and physical processes in the rarified atmosphere.

1.3 Service Spacecraft

The successful engineering of the Russian spacecraft supply vehicles is demonstrated by their continued use in servicing the International Space Station. These vehicles are launched from Earth using a Soyuz SL-4 rocket from the Baikonur Cosmodrome in Kazakhstan. The cargo spacecraft, model *Progress-M*, is of the same design as the passenger spacecraft, model *Soyuz-TM*. Both vehicles weigh 7,100 kg and measure approximately 8 x 2 meters.[6] They are equipped with autonomous navigation systems for automatic docking with the Space Station.

The *Soyuz-TM* vehicle can deliver two or three passengers to the Space Station in about three days. Designed for a round trip, *Soyuz-TM* could remain docked to *Mir* for only 200 days before requiring a return to Earth for servicing. *Progress-M* is an expendable vehicle and therefore requires no servicing. It uses a 10.6 meter long solar array to charge the power supply system batteries, which allows it to be used for extended flights or to remain on station. While

docked to the Space Station, its engines were used to alter or maintain the station's orbit. It was also loaded with waste materials over the course of its six month stay. As a replacement spacecraft neared *Mir*, P*rogress-M* separated to de-orbit and make a destructive re-entry into the atmosphere.

Each spacecraft has two identical onboard propulsion systems which use the same fuel and oxidizer. Primary propulsion is provided by a single engine, called a Progress Main Engine (PME) for simplicity. Maneuvering is provided by several paired thrusters that are scaled down versions of the PME. These thrusters comprise the Attitude Control System (ACS). Both engine configurations provide excellent sources of exhaust plume flow for monitoring.

1.4 Program Conclusion

The *Mir* Space Station was brought back to Earth after fifteen years of LEO service on March 23, 2001. By this point in its history, it had survived three times its expected lifespan, making 86,331 orbits of the earth. During this time, *Mir* had 104 space visitors from 12 countries and completed over 31,000 experiments.[7] The *MirEx* program ceased with the controlled de-orbit burn that brought the *Mir* Space Station crashing down into the Pacific Ocean. However, processing of the final *MirEx* experimental data, which observed the Space Station departure of a *Progress-M* spacecraft on April 26, 2000, (hereafter referred to simply as *Progress*) continues.

Dr. George Karabadzhak of TsN has been pursuing confirmation of molecular collision models of rocket exhaust flows in LEO with this data set.[8,9,10] He has also collaborated with Dr. Sergey Gimelshein, of the Computational Aerodynamics Lab Institute of Theoretical and Applied Mechanics, in Novosibirsk, Russia and Dr. Deborah Levin, an Associate Professor of Aerospace Engineering at Pennsylvania State University. This group has used the April 2000 data to extend existing plume models using the Direct Simulated Monte Carlo (DSMC) method.[11,12] Additionally, a team of chemists from Johns Hopkins University has used this data set for geometric modeling of molecular

potential energy surfaces. [13] These results are expected to be applied to estimations of reaction cross sections.

This last data set from the *MirEx* program has been delivered to the Advanced Missile Signature Center at AEDC for processing and final archive. Research presented will use the April 26, 2000 data to examine proposed mechanisms for the generation of excited-state OH and NH molecules. Further, the thermospheric operating environment and the importance of atmospheric mixing will be addressed when considering potential reactant collisions in spacecraft exhaust plumes.

2 Experiment

After de-docking from the *Mir* Space Station following the completion of a replenishment mission, the cargo ship *Progress* underwent dedicated flight maneuvers for observation by instruments onboard *Mir*. Approximately three and a half hours of tabulated flight data were collected during this experiment. Only the ten minute portion that occurred while *Progress* operated entirely in decelerating impulse, using its eight identical ACS motors, is utilized here.

In this chapter, the environment of low Earth orbit, in which *Mir* operated and this experiment occurs, is reviewed. Section 2.1 presents the flight geometry of the *Progress* spacecraft. In Section 2.2, the operation of the nine liquid rocket engines of *Progress* are described. Section 2.3 presents an overview of the atmosphere and the computer software program used in this experiment to model it.

2.1 Observation Method

The *Mir* Space Station occupied a LEO orbit at approximately 330 kilometers (km) in altitude; within the quasi-static temperature portion of the thermosphere's upper region. After de-docking, *Progress* decelerated from *Mir*'s orbital velocity of 7,416 meters per second (m/s) to 7,326 m/s, while descending in altitude. Note that the velocity values given here are calculated to include the correction factor for the atmosphere's co-rotation with Earth, so that all velocities are relative to a stationary atmosphere. The flight geometry, presented in figure 2, was such that the main axis of *Progress* was maintained parallel to its velocity vector. Although limited by the viewing port, *Progress* was observed tail-on as much as was possible. This required frequent manual repositioning of the imager by *Mir* cosmonauts in order to keep *Progress* in the center of the frame. Examination of telemetry data indicated that deviations from this flight geometry during the time under examination were within one degree from this viewing angle.

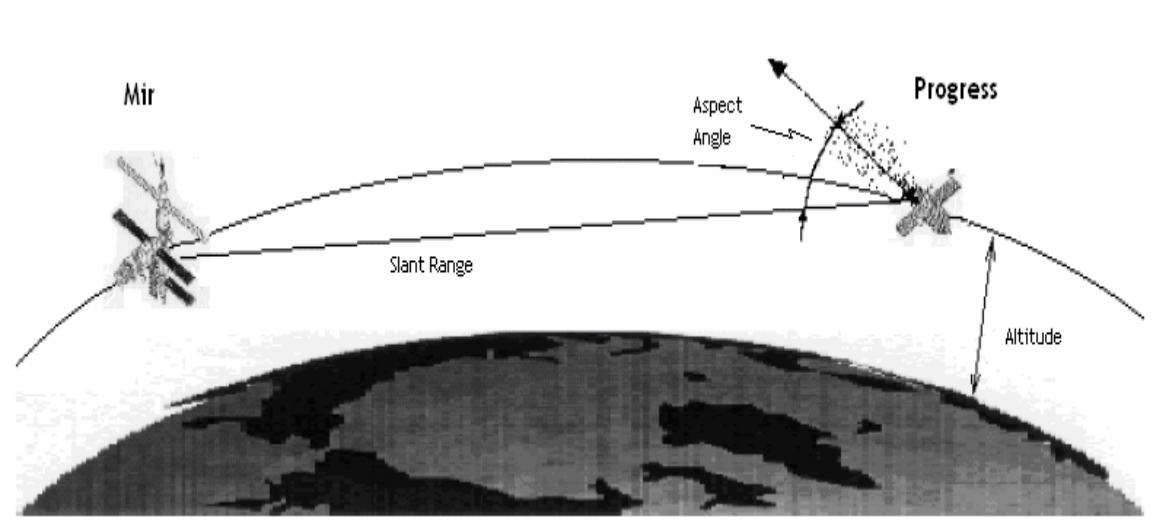

Figure 2. Viewing geometry and labeled parameters of experiment.

Figure 3 summarizes a portion of the telemetry data collected. In figure 3(a), the gradual increase in the slant range between the *Mir* and *Progress* is indicated by the change of altitudes. In figure 3(b), the time dependence of the aspect angle between the viewing port of the Space Station and the location of *Progress* is depicted. With total plume size on the order of kilometers, a slow change of viewing angle over time is imperative for retrieval of useful data from the instruments.

2.2 Engine Description

The liquid-fueled rocket engines of the *Progress-M* spacecraft each consist of an injector, a combustion chamber and a nozzle. In the walls of the combustion chamber are many small jets through which the injector forces the propellants. The jets allow the separated fuel and oxidizer to emerge as impinging vapor streams into the high pressure, high temperature chamber. It is necessary for the injected liquid oxidizer to vaporize and then mix with the vaporized fuel prior to combustion to ensure a complete reaction. [14] The nozzle, while exhausting the combustion products into space, converts the thermal/chemical energy of combustion into the kinetic energy necessary

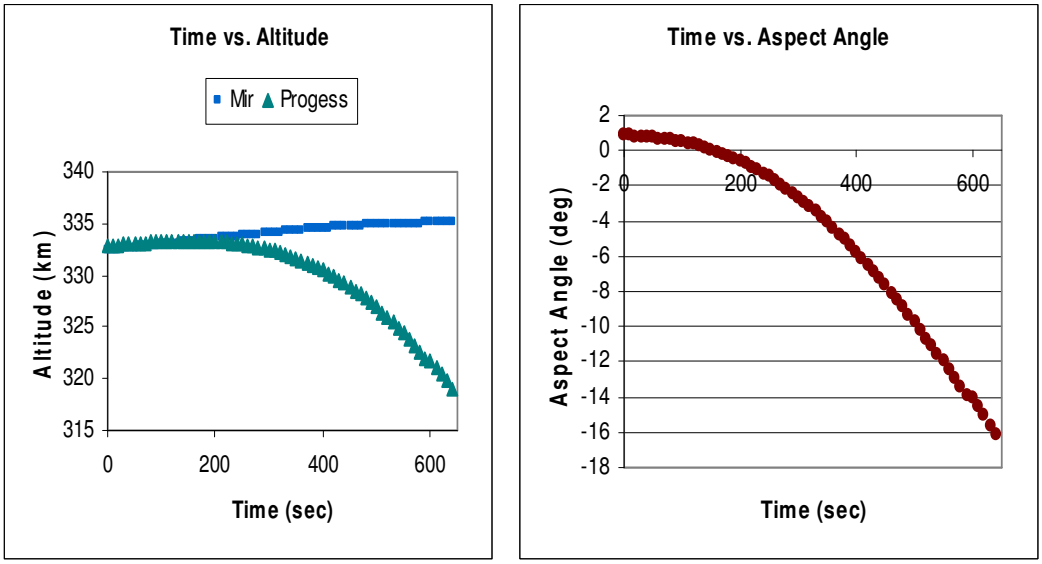

Figure 3. Summary of telemetry data.
(a) *Mir* and *Progress* altitude over time.
(b) Change in aspect angle over time.

to propel the vehicle.

After de-docking from *Mir*, *Progress* moved away from the Space Station using its centrally positioned PME. This engine had a nominal thrust of 3,100 newtons (N), or 700 pounds of force (lbf). To maneuver for a proper viewing angle from *Mir*, *Progress* used controlled firings of pairs of ACS engines. Each of the eight ACS maneuvering engines had a nominal thrust of 135 N (30 lbf). The ACS engines were tilted at a twenty degree angle toward the main axis of the craft. These engines were arranged in four pairs along the outside edge of the bottom of the vehicle, with each pair located ninety degrees from the last. A graphical representation of the engine layout is found in figure 4.

The liquid hypergolic propellant used by *Progress* consisted of unsymmetric dimethylhydrazine (UDMH) for fuel and dinitrogen tetroxide (N_2O_4) for the oxidizer. The mixture ratio of oxidizer to fuel was 1.84 by weight. The nominal flow rate through each of the eight nozzles was 0.046 kg/s for the first nine minutes of burn. This was followed by fifty seconds of burn in a fuel-rich condition. The nominal flow rate was resumed for one

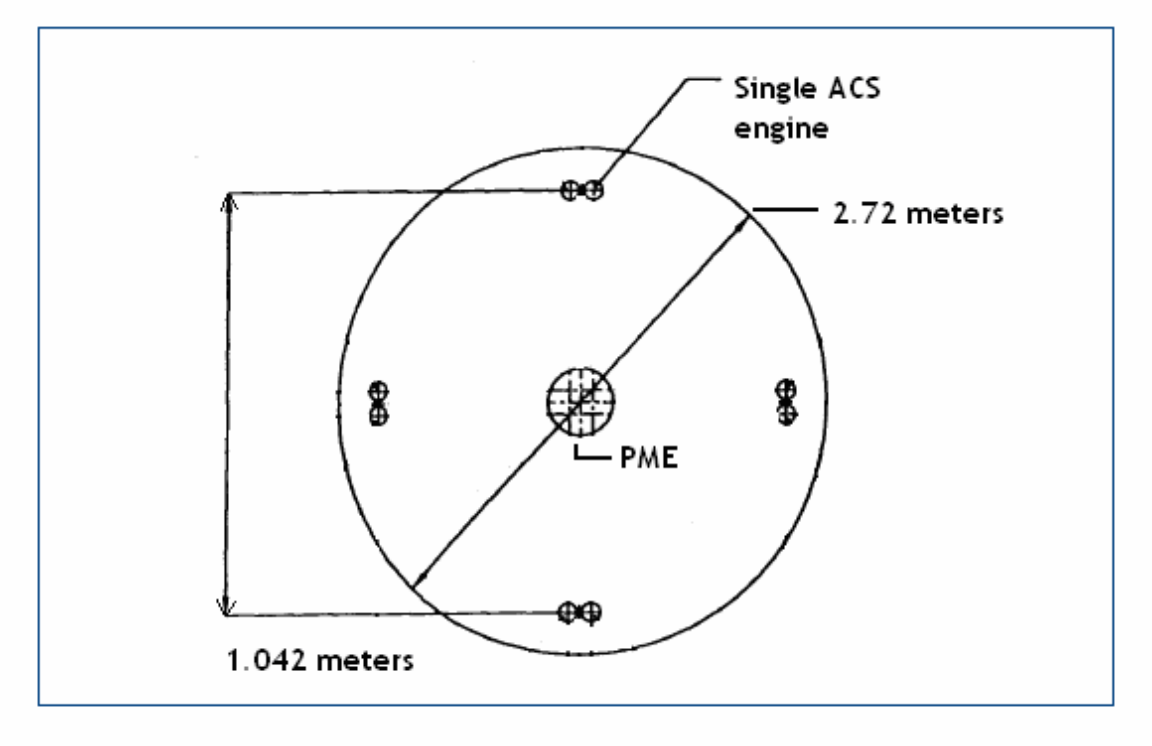

Figure 4. Engine configuration of *Progress* spacecraft.

minute, and then the ACS motors were turned off as *Progress* began its destructive re-entry.

2.3 Orbital Conditions

Earth's atmosphere is divided into several distinct regions. The field of meteorology is concerned with processes in the lower atmosphere; specifically, in the troposphere and stratosphere regions. The field of aeronomy is concerned with processes in the upper atmosphere: specifically, in the mesosphere, thermosphere, ionosphere, and exosphere regions. The focus of this experiment lies within the realms of aeronomy. It examines ultraviolet radiation from spacecraft exhaust plumes which occurred in the thermosphere and ionosphere regions. Figure 5 provides the graphical distinctions between the various levels of the atmosphere, as well as the temperature and estimated electron and major species densities at those altitudes.

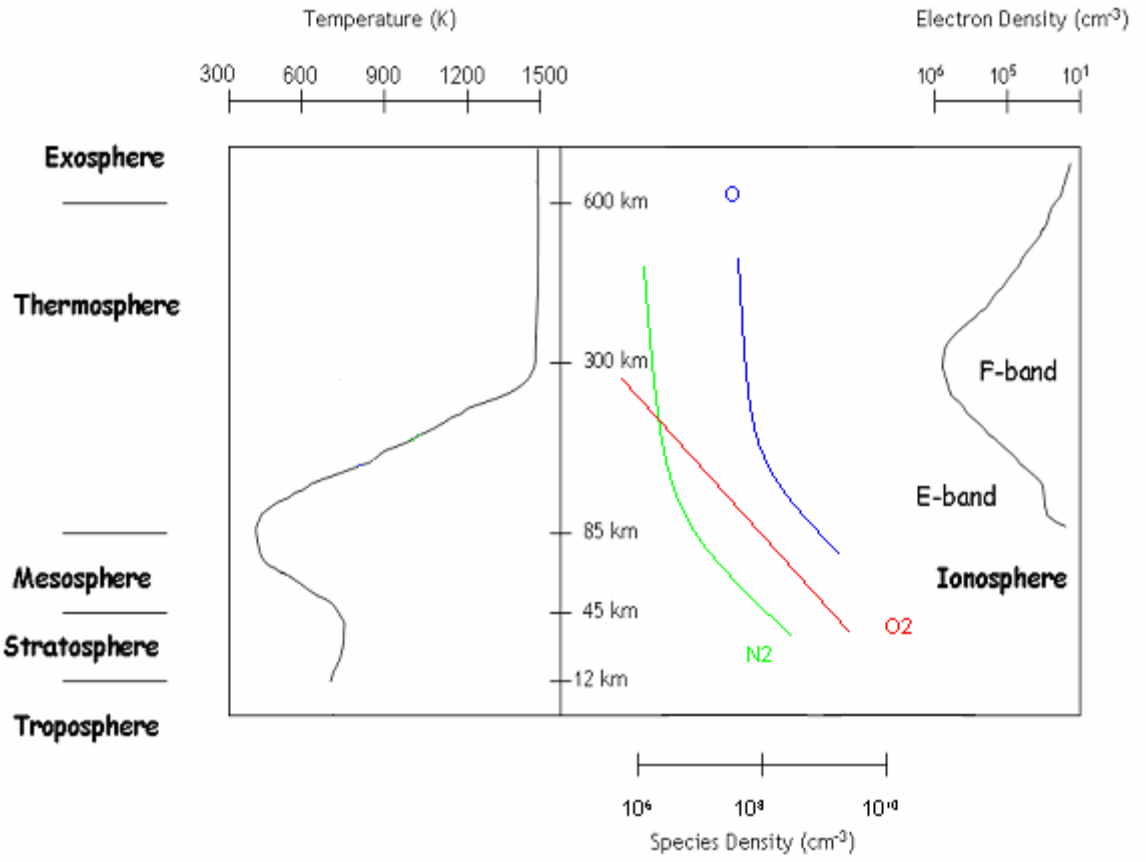

Figure 5. Earth's atmospheric regions and estimated species densities.

The thermosphere has a steep vertical temperature gradient in its lower region, but, in its upper region the temperature is independent of altitude. This region is characterized by low pressures and high temperatures. The temperature of the upper thermosphere is attributable to high energy ultraviolet light and x-rays being absorbed by the rarified gas present.[15] At this altitude, there are approximately 10^8 to 10^9 molecules per cubic centimeter, with the dominant species (representing 80-95%) being atomic oxygen.

At this altitude, energetic photons can heat the neutral gas molecules and cause ionization. This produces the region of the atmosphere known as the ionosphere. In the ionosphere there are two distinct electron density bands. The E-band has a largely neutral particle density that is mostly in photochemical equilibrium. The dominant ion species are O_2^+ and NO^+, which quickly combine with the neutral particles when sunlight is removed. In the F-band, the dominant ion species is O^+, which is not in photochemical equilibrium. Plasma transport from other atmospheric regions causes recombination of atomic oxygen ions to be highly inefficient, so they retain their ionization after the sun has passed.[16] Vertical mixing in this region, often referred to as atmospheric wind, is the result of ionized atoms and electrons which are subject to geomagnetic forces and solar radiation. Data for this study was collected at night, in the peak of the F-band region, to rule out solar effects as sources of excited-state molecules.

Chemical reactions and interactions in the upper atmosphere are difficult to simulate in a laboratory environment because the mean free paths are much greater than the apparatus dimensions. Additionally, attempts to view these processes in-situ by Earth-based test equipment are impeded by scattering from clouds and interference from the ionosphere. Remote sensing, such as that made possible by the use of satellites, is much more versatile. However, local observations, such as those possible from a space station, offer the greatest range of useful data. [17]

The plume composition is reasonably known due to the nature of the

rocket combustion (as discussed in Chapter 6). However, composition of the local atmosphere is subject to variations from solar activity and the 12-year solar cycle, as well as day-to-night variations. For this reason, these dynamic variables, along with the neutral temperature and atomic and molecular densities in the upper atmosphere, were calculated using the MSIS-E-90 (Mass-Spectrometer-Incoherent-Scatter) model.[18] Using satellites equipped with mass spectrometers, it has been possible to measure atmospheric parameters in-situ since the early 1970s. This data has been supplemented by thermospheric temperature data collected by ground-based incoherent scatter radars to produce the MSIS modeling tool. This version of the model utilizes historical measurements from flight data, ground facilities and seven satellites to extrapolate orbital conditions.

The MSIS model can estimate the temperature, mass density, and number density of individual species present in the atmosphere for one particular date, time, altitude, latitude and longitude. No actual measurements of temperature or gas density were taken during this experiment. Table 1 presents a sample listing of the MSIS modeled atmospheric parameters in one region of the space through which *Progress* traveled during observation by *Mir*. For a complete picture of the operating environment of *Progress*, the MSIS data would have to be correlated to the spacecraft flight plan. This sample is for the date April 26, 2000, at the hour of 19.5 universal time (UT), geographical latitude of 31 degrees and geographical longitude of 43 degrees.

Table 1. Sample of MSIS modeled characteristics for major species.

Altitude (km)	Number Densities			Mass Density ($g*cm^{-3}$)	Temperature (K)
	O (cm^{-3})	N_2 (cm^{-3})	O_2 (cm^{-3})		
320	6.99E+08	1.19E+08	3.65E+06	2.47E-14	1094.7
322	6.78E+08	1.12E+08	3.43E+06	2.38E-14	1094.9
324	6.57E+08	1.06E+08	3.22E+06	2.30E-14	1095.2
326	6.37E+08	1.01E+08	3.03E+06	2.21E-14	1095.4
328	6.17E+08	9.53E+07	2.84E+06	2.13E-14	1095.6
330	5.98E+08	9.03E+07	2.67E+06	2.06E-14	1095.8
332	5.80E+08	8.55E+07	2.51E+06	1.99E-14	1096
334	5.62E+08	8.09E+07	2.36E+06	1.92E-14	1096.2

3 Test Equipment

In the last half of the 1990s, the launch cost to place one kilogram of test equipment into orbit was approximately $20,000.[19] For this reason, it was obvious that utilizing the equipment already in orbit would be very economical. Over the course of the three years that *MirEx* was in operation, the US government spent a total of only $560,000 on the program. This is an astoundingly small amount of money to spend for the ability to conduct experiments in space.

This chapter examines the instruments used to fulfill the *MirEx* program. Section 3.1 follows the change of conditions onboard *Mir*. In Section 3.2, an overview of the test equipment co-alignment is given. Section 3.2.1 gives a description of the spectrometer purchased for *MirEx* by AEDC, while Section 3.2.2 describes the imager provided by TsN. Section 3.3 demonstrates the difficulties in returning the test data to analysts on Earth.

3.1 Original Plan

A complete review of the eleven tons of research equipment onboard *Mir* resulted in the selection of three basic instruments for use in the *MirEx* program. Those instruments were a UV imager, an ISTOK IR spectrometer, and a BRIZ vacuum ultraviolet/ultraviolet (VUV/UV) spectrometer. The imager was located in the *Core* module and controlled by cosmonauts. The BRIZ spectrometer was located externally on *Spektr*, while the ISTOK IR spectrometer was located externally on *Priroda*. Both spectrometers were operated by telemetry up-linked programs from Mission Control Center via an onboard control unit.

On June 25, 1997, a *Progress* spacecraft (number M-34) collided with *Spektr* while attempting to dock with *Kvant-1*. The collision damaged solar panels and punctured the hull of *Spektr*, causing it to depressurize. The *Spektr* module was sealed off to preserve the integrity of the rest of the station. The

IR spectrometer positioning mechanism was damaged, as well as the VUV/UV spectrometer. This mishap caused a re-evaluation of the *MirEx* program goals. It was determined that experimentation would continue on *Mir*, with study focused on plume behavior in the ultraviolet region of the spectrum, using other instruments from the *Core* module.

3.2 April 26, 2000 Instrumentation

The UV imager, developed for *Mir* by TsN with the assistance of Lebedev Physical Institute,[20] was undamaged in the collision. A replacement, however, was needed for the UV spectrometer. AEDC purchased two ultraviolet-near infrared (UV-NIR) spectrometers. After calibration of both instruments, one unit was placed in a ground-training facility for familiarization by cosmonauts, while the other was sent up to *Mir* in February of 1998 on a *Progress* mission.

The fiber-optic focusing lens of the spectrometer was rigidly fixed to the imager in order to co-align the field of view (FOV) of both instruments. The imager had a 3-axis gimbaling mount which provided rigid mounting to the frame of a quartz viewing port in either *Priroda* or *Core*. For this experiment, window number 9, located in the *Core* module, was used. Figure 6 shows this co-alignment, with the inner ring drawn to represent the spectrometer 2.6 degree circular FOV and the outer ring representing the imager 9.8 degree circular FOV. This unprocessed image clearly shows the exhaust plume of *Progress* in the center of the frame. Also visible in the raw image are the time-stamp, in the lower right corner, as well as numerous stars and bad pixels throughout the image.

Both instruments were manually operated by *Mir* cosmonauts based upon direction from scientists at Mission Control Center in Russia. Image data was captured on BetaCamSP Professional videotapes in standard analog format using a commercially-available Sony 8mm camcorder. The imager acquired data was constrained by the camcorder frame rate of 25 frames-per-second to a temporal resolution of 0.04 seconds.

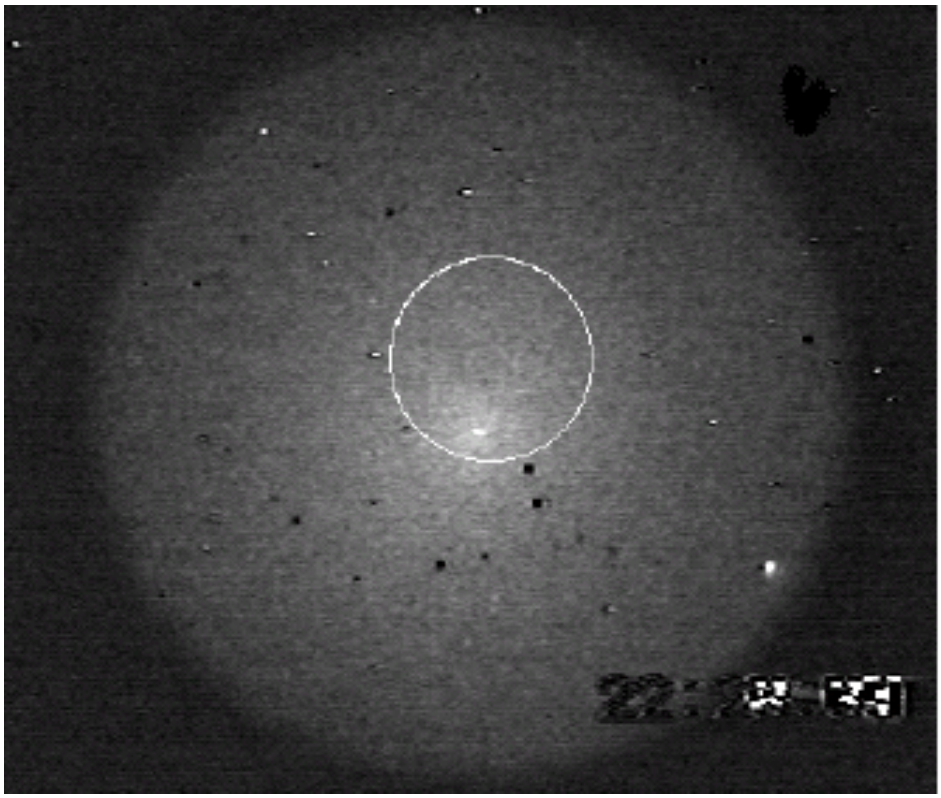

Figure 6. Sample of raw video obtained April 26, 2000. The white circle indicates the spectrometer FOV.

3.2.1 UV-NIR Spectrometer

The OceanOptics S2000 model (UV-NIR) spectrometer weighed less than a pound. It had a 600 micrometer entrance aperture with a 5 mm ultraviolet-grade focusing lens. It was connected via a fiber-optic cable to a high-speed A/D card in a Toshiba Satellite Notebook computer for control of data acquisition. The basic characteristics of the spectrometer are summarized in table 2.

3.2.2 UV imager

The UV imager consisted of a radiation detector interfaced by a relay lens and an image intensifier. The input was captured by a quartz F/1 aperture telescope with a permanently attached broad-band color glass UV filter that was mounted to the interior side of the viewing port. Additionally, three narrow-band interference filters were installed on the telescope by cosmonauts. While the broad-band filter provided off-band blocking of visible and near-ultraviolet radiation, the narrow-band filters provided specific waveband selection in the mid-ultraviolet region.

The UV image intensifier had circular geometry and used a solar-blind cesium telluride (Cs_2Te) photocathode to effectively block the visible radiation.

Table 2. Specifications of the OceanOptics S2000 spectrometer.

Specifications	Range
Wavelength region, nm	178-878
Number of channels	2048
Digitization level, bits	12
Spectral resolution, nm	8-10
Angular Field of View, μrad	45375
Minimum sampling time, sec per spectrum	~ 0.02
Dynamic range, single sample	~ 500

The intensifier output was viewed by a standard rectangular charge coupled device (CCD) detector. This is the reason that the illumination occupies a circular region in the center of figure 6. The basic characteristics of the imager are summarized in table 3.

3.3 Data Handling

The initial video feed and digital spectrometer data were sent by telemetry link to Russian analysts on Earth. This allowed preliminary analysis on the data to begin while awaiting the return of the original videos to Earth with the next crew change. It was found, however, that the telemetry introduced a significant amount of noise to the imager data.[21, 22] Because the spectrometer data was already in digital form, it was qualitatively unchanged by the telemetric transmission. The images used here were obtained from copies made of the original video tapes. The tapes were returned to Earth, via the spacecraft *Soyuz* (number TM-30) on June 13, 2000, with the departure of the final crew to man the *Mir* Space Station.

Table 3. The UV imager general characteristics.

Specification	Range
Operating wavelength region, nm	200 - 360
Wide band color UV filter, nm	240 - 360
Interference filters centers, nm	260, 284, 315
Telescope effective diameter, mm	55
Telescope focal length, mm	78
Field of view, degrees	9.8
Angular resolution, μrad	~1308
Maximum sensitivity, W/cm2 per count	~ 2×10^{-17}

4 Spectral Data

This chapter takes a closer look at the data collected by the UV-NIR spectrometer. Section 4.1 follows the progression of processing of the raw spectroscopic data. In Section 4.2, the spectral data is extracted from the raw data in order to determine the primary emitters present in the plume.

4.1 Processing

During the April 26, 2000 event, the OceanOptics spectrometer collected 330 data samples in approximately 2.5 second intervals. This research considered only the ten minutes that coincided with the ram-burn of *Progress* ACS engines for analysis. These data samples represent the intensity at each of the discrete 2,048 wavelengths, between 178.4 nm to 878.4 nm, monitored by the spectrometer. In-flight calibration of the spectral response of the spectrometer was performed using the Moon as the radiation source.

Computation of the modeled spectra was accomplished by convolution of the Moon albedo with the solar spectrum. This process took into consideration the date and time of the collection to determine the phase of the Moon and the solar radiation it received. The spectrometer was found to be most sensitive to visible light, with deviations of up to 15% from the laboratory calibrated response values occurring in the wavelength region from 680 nm to 800 nm. However, in the 240 nm to 360 nm region considered here, deviations were less than 5%. Spectrometer response values can be found in their entirety in reference 9.

The raw spectrometer data was received at AEDC as an ASCII text file in units of counts. For a first look at the data, it was imported into an *Excel* file for manipulation. Due to the weak signal present, this effort produced little in the way of usable results. The next attempt to visually represent the data was made utilizing the computer program *Matlab*, a comprehensive mathematical software tools package.[23] A three dimensional surface plot was used to

represent the raw data, with interpretive shading that indicated minimum count values in blue and maximum count values in red. This unprocessed surface plot is shown in figure 7(a). This graphic makes it evident that there were numerous saturated channels within the visible light wavelengths of the spectrum throughout the collection interval. Additionally, the spurious peaks across all wavelengths give indication of a significant amount of random noise being present.

For comparison to the imager data, the raw spectra within the wavelength region of 240 nm to 360 nm, which is contained within the red box of figure 7(a), was extracted from the complete surface plot for analysis. The extracted UV region of raw data was automatically rescaled by *Matlab*, and is shown in figure 7(b). The maximum counts for this spectral region have now become the red band. At this point, there appear to be two peaks, closely spaced in wavelength, separated by approximately 20 nm from a less intense peak signal. Efforts were initiated to reduce noise and extract intelligence from this spectra, in order to determine the radiating species present.

4.2 Data Analysis

The initial assumption was made that the number of photons at each of the discrete wavelengths detected by the spectrometer is indicative of the concentration of emitters present. However, the detected signal strength of the individual samples was too weak to draw quantitative conclusions about the particular wavelengths observed. Various methods and repeated unsuccessful attempts were made to extract usable data from the raw spectra. The goal was to duplicate for the 240 nm to 360 nm region the signal processing efforts described by Karabadzhak in reference 9. His processing began with averaging of samples over 30-40 second intervals and then integrating over 10-12 nm bandwidths. The signal-to-noise ratio was to be improved by background subtraction followed by FFT-smoothing procedures.

Unfortunately, when this process was performed on the AEDC dataset, a

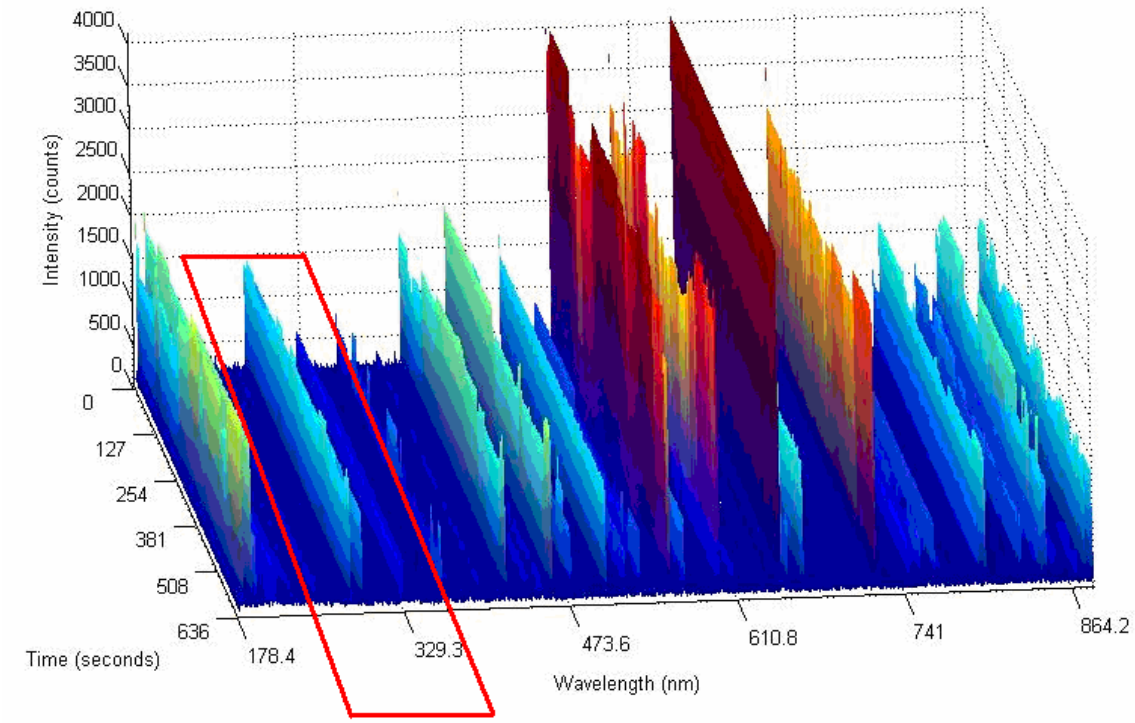

(a) Raw complete spectra

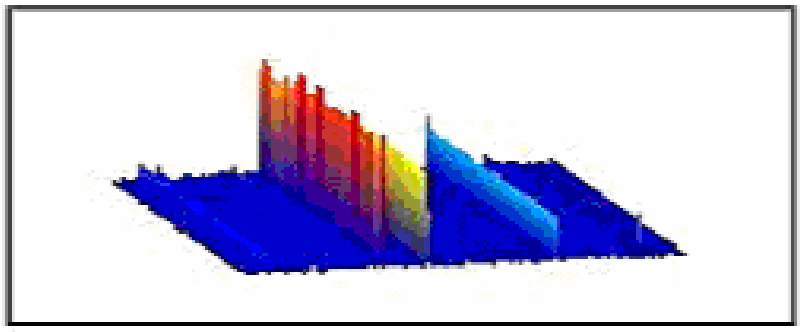

(b) Raw spectra from the boxed region above

Figure 7. Surface plot of raw spectrometer data.
(a) Wavelength region from 178.4 nm to 878.4 nm
(b) Wavelength region from 240 nm to 360 nm

usable spectrum could not be produced. This is demonstrated by the sample of processing performed on the entire spectrum that is shown in figure 8. Here it is seen in figure 8(a) that the sample averaging and integration technique produced distinct peaks in the spectrum while magnifying the significant noise. Subsequent smoothing removed the distinguishing features from the spectrum, as is shown in figure 8(b). Repeated attempts produced no better results.

Using the described method, Karabadzhak was able to recover usable qualitative spectrometer data in the 300 nm to 775 nm range only. The composite spectrum, seen in figure 9, shows the primary emitters detected in the *Progress* exhaust plume within this wavelength region. The in-flight calibrated response is applied to the spectrum, thus the intensities of the emitters given are absolute values. The peaks indicating the radiation of OH ($A\ ^2\Sigma^+ \rightarrow X\ ^2\Pi$) at 306-315 nm, and NH ($A\ ^3\Pi \rightarrow X\ ^3\Sigma^-$) at 335-336 nm also fall within the operating region of the UV imager, where further separation of the data can occur.

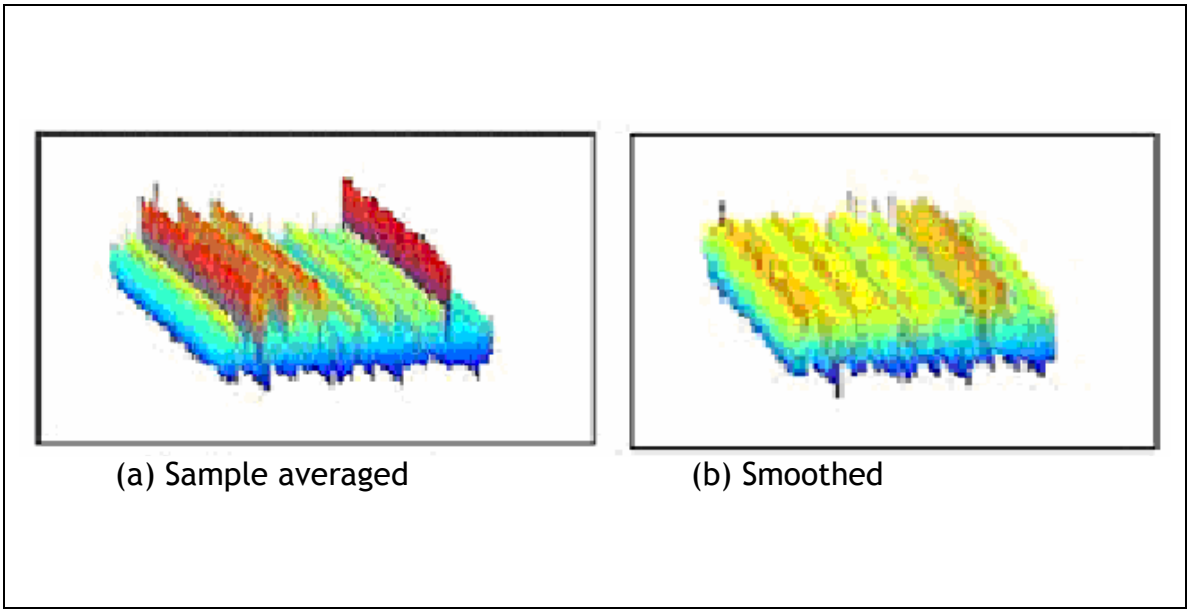

(a) Sample averaged (b) Smoothed

Figure 8. Processed and smoothed spectrum.
(a) Results of sample averaging
(b) Results of smoothing

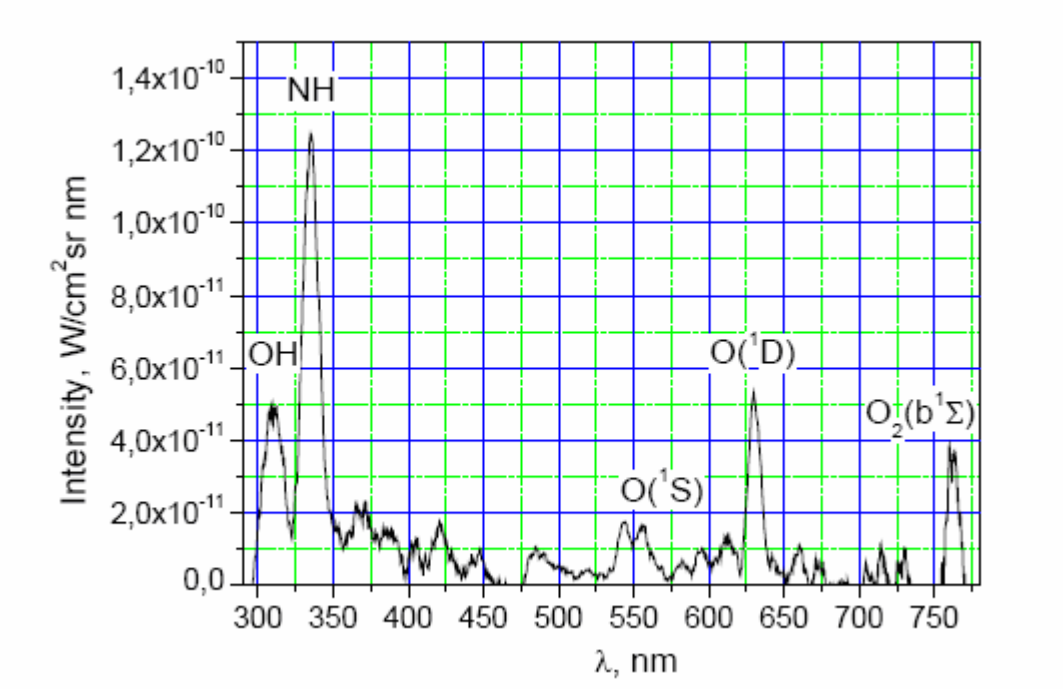

Figure 9. Composite spectrum derived from spectrometer data. *Taken directly from Reference 9.

5 Imaging Data

This chapter takes a closer look at the data collected by the UV imager. Section 5.1 follows the progression of processing of the visual data. Section 5.2 presents the calibration process performed by Russian scientist using data gathered by cosmonauts prior to beginning this experiment. In Section 5.3, analysis is given of the data retrieved during image processing.

5.1 Image Processing

A DC30+ commercial video board was used by TsN to provide an 8-bit level digitization of the Video8/PAL data. Over 21,000 frames of 768-by-576 pixel, gray-scale bitmap images were collected during this experiment. For ease of manipulation, these files were first converted into Standard Archive Format (SAF). SAF is a file-format program designed by the Advanced Missile Signature Center (AMSC) at AEDC for easy image data extraction. The SAF files were then made into movies of the entire test. Image registration of the individual frames, with time-stamp removal, was attempted using three *Matlab* methods: co-adding sequential SAF images, transform of bitmap images, and use of a locally developed graphical user interface (GUI) tool. A visual comparison of the first two methods is shown in figure 10.

Co-adding of SAF frames was accomplished through several tools found in the SAF Toolbox group of routines written by AMSC software engineers specifically for use with *Matlab*. Because SAF added blocks of ASCII formatted characteristic data about the image, a special routine was used, called *DVRead,* which ignored these lines of information. The frames were then stacked directly upon each other, with the resultant image seen in figure 10(a). This tool was very convenient because it could be used on standard format files. However, the stacking of images needed to be confined to a small series of frames, in which relatively little motion of the target occurred, in order to minimize the size of saturated areas caused by bad pixels.

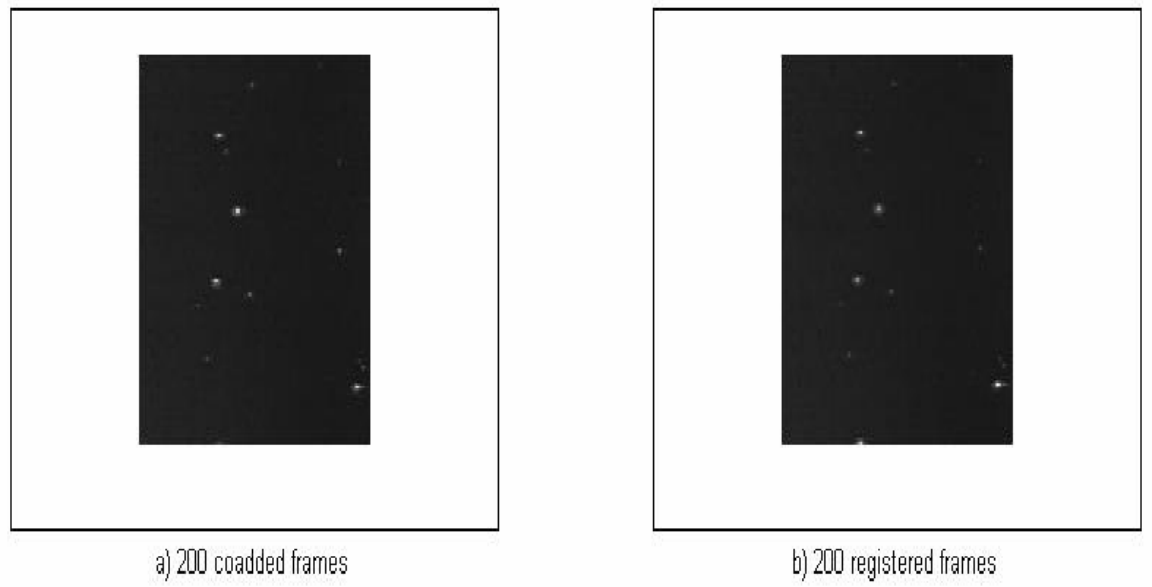

Figure 10. Example of the results of two image registration methods.
(a) Consecutive addition of 200 individual images.
(b) Transformation of 200 individual images.

The transform function was part of the Imaging Processing Toolbox group of routines available in *Matlab*. The bitmap images were imported to the workspace and an anchor frame, in which *Progress* had a centralized position relative to the rest of the frames, was selected. Several reference points were selected from this frame using the *cpselect* command. Using the *cp2tform*, and the *linear conformal* format commands, the processor searched the target frame for the reference points. The result was a series of new images, each stacked on the anchor frame with the reference points coinciding. These images were then registered with the *imtransform* command. While effective for keeping the frames aligned, this tool tended to blur the image, as is evident in figure 10(b).

The last image registration method used was a GUI developed by the AMSC under the direction of Dr. Bob Reed. A snapshot of the stages in the processing of the plume image is presented in figure 11. The GUI used a combination of the above methods to produce registered images of long series of SAF files. In transforming the files, this routine used the location of *Progress*

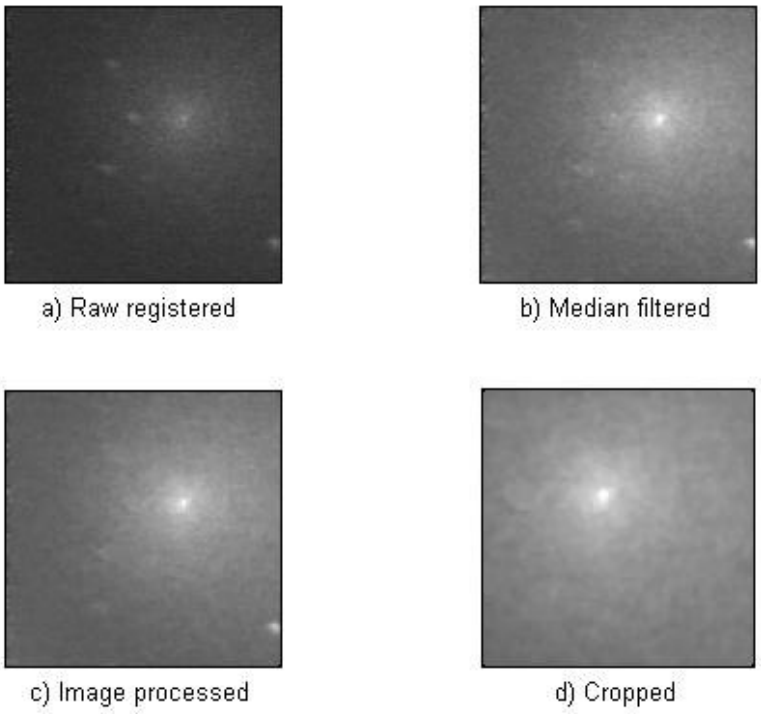

Figure 11. Gray-scale image processing progression.
(a) GUI generated registered raw image compiled from 200 individual frames.
(b) Median filtered registered image at 256-by-256 pixel size.
(c) Processed registered image at 256-by-256 pixel size.
(d) Plume image cropped to 150-by-150 pixel size.

as the anchor in each frame. The image shown occurred at 155 seconds after initial ACS engine firing.

The file series were each converted to a single 256-by-256 pixel image, with additional data files generated for the tracked motion of *Progress* and compiled characteristic information. Correction of bad pixels was accomplished using a nearest neighbor replacement. A mask matrix composed of stars and uncorrectable bad pixels was next constructed. This mask was then multiplied by the GUI generated image matrix to produce a raw, registered image. Further image processing was accomplished using standard *Matlab* routines; including median, image and convolution filtering.

Because of the versatility and accuracy of the GUI it became the primary tool used to register the raw image frames. To enhance the details of the plume, the GUI generated figures were converted to pseudo-color images. As can be seen in figure 12, the plume boundaries are now clearly visible, where relative intensity increases from the blue to red regions. As the ACS engines fire (from left to right in the image), the most intense region of the plume is observed to trail to the right. Additionally, the direction (from right to left in the image) of the significantly slower atmospheric wind becomes evident with the plume dispersion in the opposite direction of the exhausted combustion products. Note also, that the actual physical location of *Progress* is to the left of the observed plume field.

5.2 Calibration

This imager was used throughout the years of the *MirEx* program. This allowed calibration over a variety of radiance levels using numerous stars; with particular attention paid to single pixel and integral point source responses. The imager angular resolution was found by analyzing images of point sources located at infinity. In this experiment, those point sources were stars in the Pyxis and Puppis constellations. The single pixel angular dimension was found to be 342 μrads at both the center of the image and at the edge. This

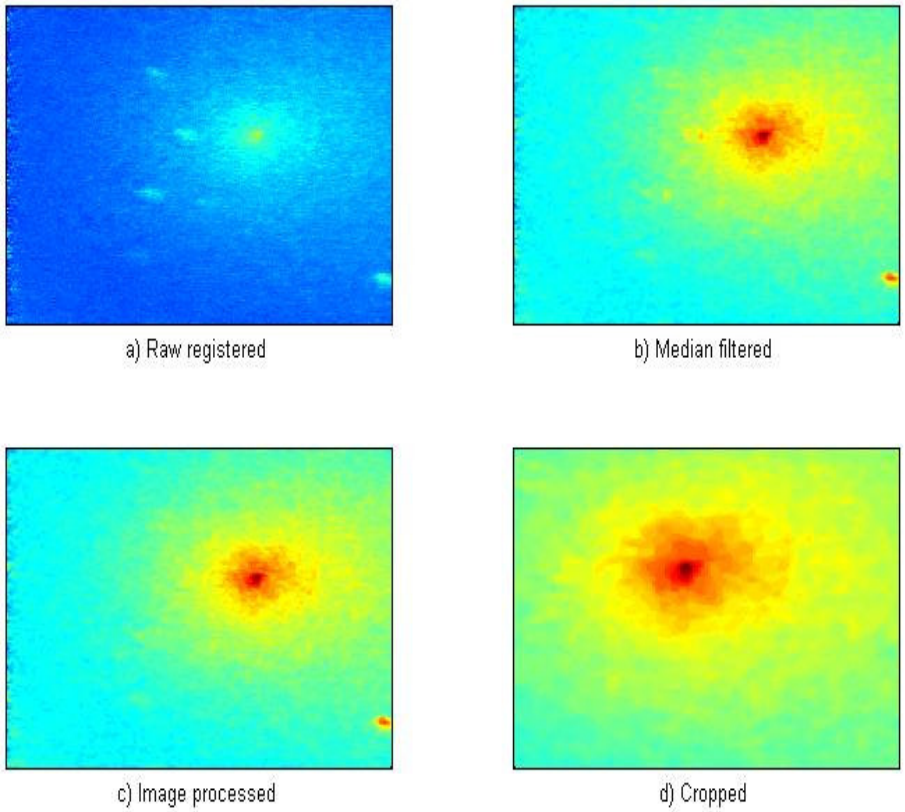

Figure 12. Pseudo-color image processing progression.
(a) GUI generated registered raw image compiled from 200 individual frames.
(b) Median filtered registered image at 256-by-256 pixel size.
(c) Processed registered image at 256-by-256 pixel size.
(d) Plume image cropped to 150-by-150 pixel size.

represents the minimum picture element fixed by digitization of the video signal. For a non-saturating point source response, the imager angular resolution measured approximately 0.08 degrees at full-width, half-maximum.

To measure the uniformity of response of the imager FOV, cosmonauts took a series of images of a single star. In each image, the star appeared in a different place in the picture. A decrease in response was detected at the edge of the FOV only. Additionally, the imager absolute response is strongly dependent upon the *Mir* window transparency. Changes in both the absolute sensitivity and the relative spectral sensitivity are possibly due to attenuation of radiation passing through the window. A change in the absolute transparency of the window was found, attributable to time and wear, which necessitated a correction of the imager response curve. The window/imager system absolute response value was calculated by Karabadzhak (Ref. 9) to be 4.8×10^{16} counts per W/cm^2 by using the observed star irradiances. Figure 13 is a graph of the calculated absolute spectral response for the April 26, 2000 data collection.

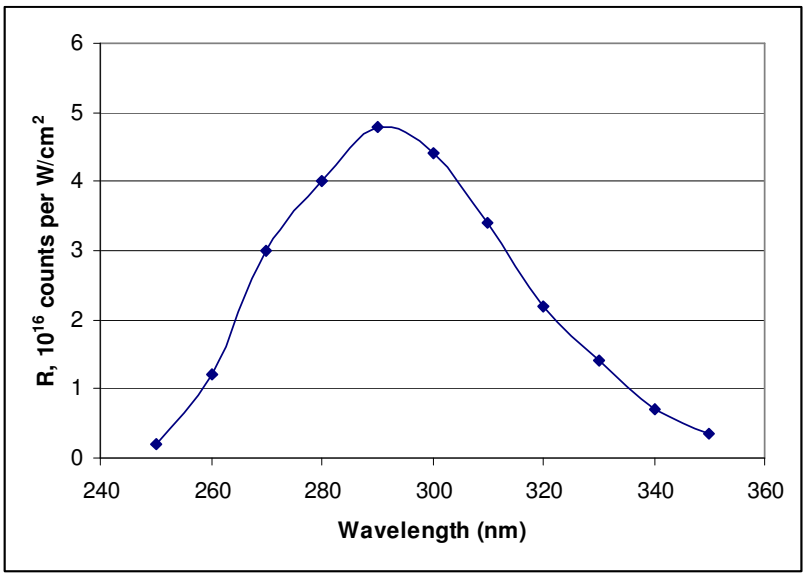

Figure 13. Absolute response of the imager/window system.

5.3 Image Analysis

The cropped frame of the GUI-registered composite image measured 150-by-150 pixels. This corresponded to an effective imager FOV of 2.88 degrees during this time. An image radial profile of the cropped frame was calculated using a *Matlab interp2* command-based subroutine. To visualize the radial profile of the near-field plume at various points throughout the entire ACS engine firing, the *Matlab* data was imported into Microsoft *Excel* in order to construct a graph. The plot seen in figure 14, shows the radial development of the total radiant intensity of the plume at four different times during the experiment. As expected, the plume radiates more intensely early into the firing, and becomes more diffuse and less intense as firing continues. Here the expanse of plume covered by a single pixel width at each time snapshot is shown in the displacement of the starting integral from zero.

Considering the imager preferential sensitivity to the OH ($A\ ^2\Sigma^+ \rightarrow X\ ^2\Pi$) emission wavelength, the goal of this observation turned to

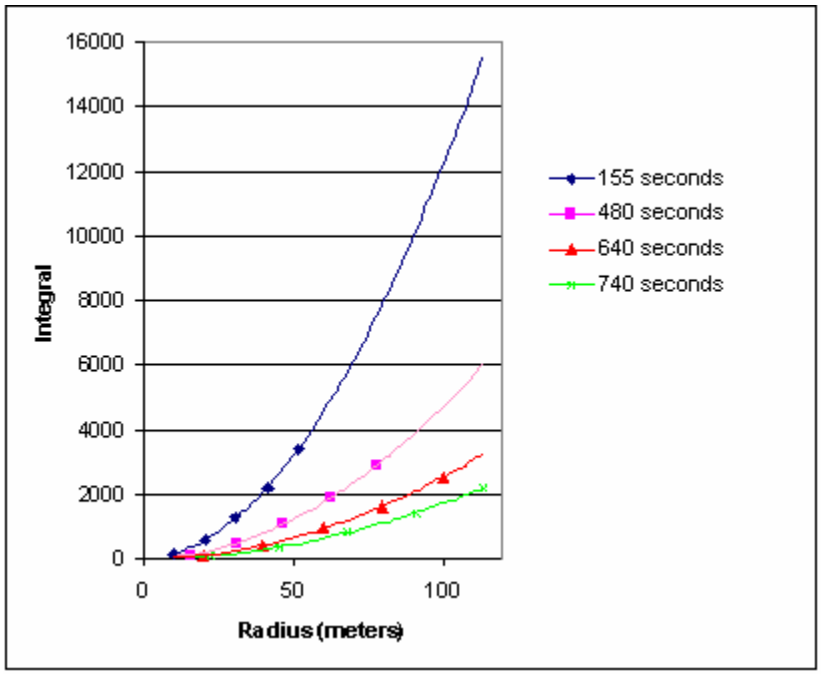

Figure 14. Snapshot of radial integral behavior at various distances.

separating out the NH ($A\ ^3\Pi \rightarrow X\ ^3\Sigma^-$) contribution from the input data. At approximately 157 seconds into engine firing, cosmonauts manually installed onto the imager lens the third of three narrow-band filters available. At a band-pass of 315 nm (±9 nm), the filter effectively blocked the contribution of NH ($A\ ^3\Pi \rightarrow X\ ^3\Sigma^-$) to the imager received signal. Because the filter covered only the imager's input lens, it left the spectrometer signal unimpeded. Figure 15 offers a visual comparison of the processed GUI registered images taken directly before and directly after the installation of the narrow-band filter, using the same scaling.

Comparison of the images in figure 15 makes several key points apparent. First, the most intense portion of the original UV radiation detected by the imager within the ACS exhaust plume resulted from NH ($A\ ^3\Pi \rightarrow X\ ^3\Sigma^-$) transitions. Second, the OH transitions occurred at a significant distance from the rocket. Considering the radiative lifetimes of the excited molecules, 0.69 microseconds for OH ($A\ ^2\Sigma^+$) and 0.43 microseconds for NH ($A\ ^3\Pi$), it has been assumed that each species will transition to their respective lower energy species at the same point in space at which they radiate.[24] Thus, the image processed after the filter was installed appears to confirm that the NH ($A\ ^3\Pi \rightarrow X\ ^3\Sigma^-$) radiation occurred closer to the spacecraft than the OH ($A\ ^2\Sigma^+ \rightarrow X\ ^2\Pi$) radiation.

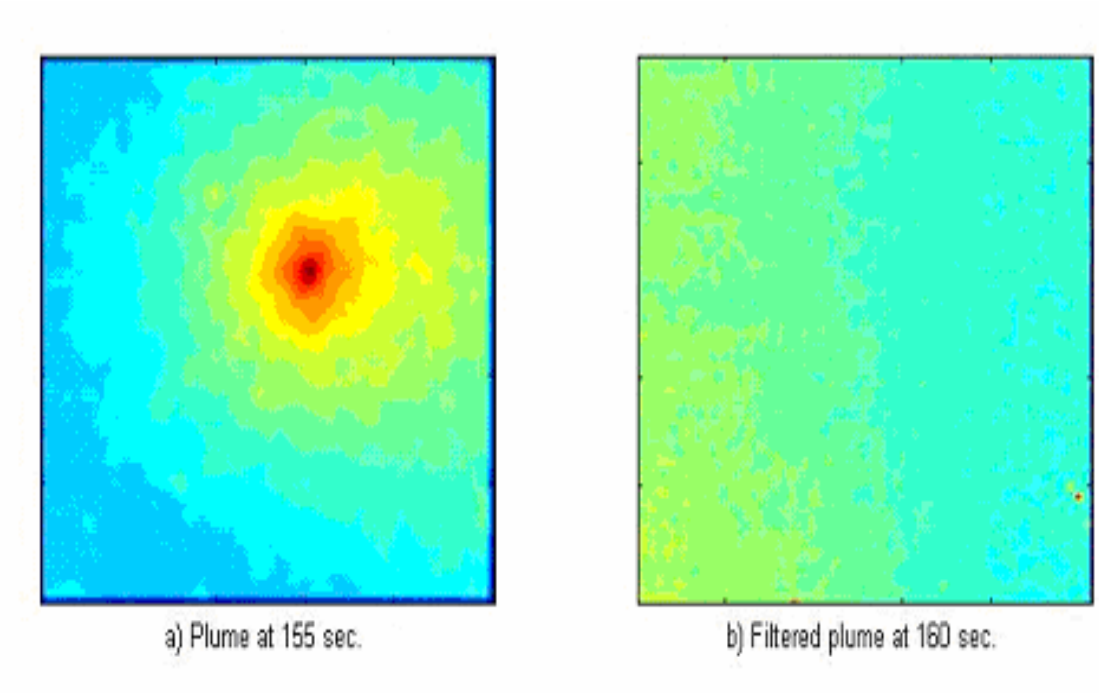

Figure 15. Processed plume images.
(a) Before 315 nm narrow-band filter installation.
(b) After 315 nm narrow-band filter installation.

6 Excitation Mechanisms

Chemiluminescence is the release of energy, in the form of light, which occurs as an electronically excited molecule relaxes to the ground state. Unlike phosphorescence or fluorescence, chemiluminescence does not require the excited molecule to first absorb light energy to reach the excited state. The energy required to put the molecule into an excited state originates in a chemical reaction. The observed radiation in this experiment was a result of the chemical reactions that occurred when the combustion gases produced by the *Progress* ACS engines collided with the ambient species present in the atmosphere. These collisions then produced electronically excited OH and NH molecules which spontaneously returned to their ground state through the emission of radiation.

In this chapter, several potential chemical mechanisms for the observed radiation are discussed. Section 6.1 looks at the exhaust plume effluents in order to propose sources for the OH (Section 6.1.1) and NH (Section 6.1.2) excited-state molecules. Section 6.2 develops values for the energy available via collision (Section 6.2.1) and the energy necessary (Section 6.2.2) for each reaction to proceed. Section 6.3 presents the chemical kinetics of this experiment through equation development (Section 6.3.1) and collisional cross section considerations (Section 6.3.2), to propose a model for the collected *MirEx* data.

6.1 Proposed Mechanisms

To determine the amount of each product expected at the LEO conditions modeled by MSIS-90, another software package is used. Numerical Analysis of Real Jets (NARJ) is a tool used for simulating combustion products from chemical propulsion engines.[25] It incorporates numerous Fortran programs for laminar and turbulent mixing, phase change kinetics, and physical/chemical dynamics of reactions.

When a stoichiometric mixture of the oxidizer dinitrogen tetroxide and the fuel UDMH completely react they produce the gaseous products of nitrogen, water vapor and carbon dioxide according to equation 1.[26]

$$(CH_3)_2N\text{-}NH_2\ (l) + \frac{3}{2} N_2O_4\ (l) \rightarrow 5\ N_2\ (g) + 4\ H_2O(g) + 2\ CO_2(g) \qquad (1)$$

By dividing the oxidizer molecular weight of 138 grams per mole, by the molecular weight of 60.09 grams per mole of the UDMH, the oxidizer to fuel (O/F) ratio of the stoichiometric mixture is found to be 2.3. *Progress*, however, used an (O/F) ratio of 1.84 (by weight) to produce the maximum thrust. Thus the product ratios of the above equation no longer apply.

To correctly calculate the reaction of UDMH fuel in a single *Progress* ACS engine at this O/F ratio, the NARJ program was used. The NARJ generated characteristics of this reaction, occurring at the nozzle of a single ACS engine, are a flow velocity of 2818 m/s, and gas density of 2.69×10^{-3} kg/m^3 per second, pressure of 637.6 Pa, and temperature of 591.4 K. The NARJ generated products of the chemical reaction in equation 1 are listed in table 4.

Table 4. NARJ calculated values of major exhaust constituents.

EFFLUENT SPECIES	MOLE FRACTION
H_2O	0.293
N_2	0.267
N	5.4×10^{-8}
NO	3.4×10^{-4}
CO	0.193
H_2	0.188
H	8.5×10^{-3}
CO_2	0.049
O_2	2.7×10^{-5}
OH	2.8×10^{-5}
O	1.4×10^{-5}

6.1.1 OH

With water as the major constituent of the plume exhaust, as indicated in table 4, its collision with the ambient atmosphere is a likely source for the excited state hydroxyl (OH ($A\ ^2\Sigma^+$)) molecules. Equation 2 presents the hypothesis suggested by Karabadzhak, et al, for the generation of OH ($A\ ^2\Sigma^+$) from the gaseous reaction of water and atomic oxygen.[27]

$$O\ (^3P) + H_2O \rightarrow OH\ (A\ ^2\Sigma^+) + OH\ (X\ ^2\Pi) \quad (2)$$

This is an endothermic process. The reaction threshold is the energy required to break one of the O-H bonds in the water molecule. The value of this threshold is 4.8 eV.[28]

6.1.2 NH

A source for the NH ($A\ ^3\Pi$) molecules cannot be found in a single collision model with any of the species listed in table 4 and atomic oxygen. Reaction modeling, such as that used in the NARJ code, assumes that a complete reaction occurs in the combustion chamber of an engine. However, in test cell measurements of rocket exhaust plumes, the presence of unburned fuel has been indicated. [29] Thus the hypothesis suggested for NH ($A\ ^3\Pi$) formation in the exhaust plume by Viereck, et al, is the presence of unburned fuel components reacting directly with the ambient atmosphere.[30]

Neither the specific chemical composition of the unburned fuel fragments, nor the amount present in the plume, is conclusively known. However, an accepted generalized global chemical process is presented in equation 3.[4,10,17,29]

$$O\ (^3P) + UDMH \rightarrow NH\ (A\ ^3\Pi) + products \quad (3)$$

This reaction has been extensively studied, with no definitive conclusion agreed upon.[31,32] Therefore, this work will consider two different mechanisms for the generation of excited-state NH. These reactions involve the ambient atmospheric atomic and molecular nitrogen with the gaseous water exhaust

product, as in equations 4 and 5.

$$N + H_2O \rightarrow NH\ (A\ ^3\Pi) + OH\ (X) \quad (4)$$

$$N_2 + H_2O \rightarrow NH\ (A\ ^3\Pi) + OH\ (X) + N \quad (5)$$

Table 5 returns to the MSIS-90 derived atmospheric constituents seen in Chapter 2. Like table 1, this sample is taken on the same date, at the same time, altitude, and geographic location. Table 5, however, is a sample of the MSIS calculated minor atmospheric constituents present. While the atomic nitrogen density is 100 times less than that of the major species of atomic oxygen and molecular nitrogen found in table 1, there is still a significant amount of the element present to react. Therefore, the reaction proposed in equation 4 warrants consideration.

6.2 Energetics

It has been confirmed that the OH and NH emission radiant intensities from exhaust plumes are dependent upon the ram angle of the engine firing.[11,24] Maximum intensities have occurred when the exhaust effluents exited the nozzle at a 180 degree angle to the atmospheric wind. Radiant intensity for both species have been observed to decrease as the angle decreased; becoming undetectable at 90 degrees. This dependence on the cosine of the collision angle between reactants indicates that a significant energy threshold must be overcome to form either radiating species. It must be noted that the NH emission intensity is also dependent upon the liquid rocket fuel used.[31,32] The strongest observed radiations from NH ($A\ ^3\Pi \rightarrow X\ ^3\Sigma^-$) have occurred with UDMH fuel at full-ram conditions.

Progress had an average velocity of 7,382 m/s in low Earth orbit. In addition, the average plume exit velocity from the nozzle was 2,818 m/s. This produced an average relative velocity of 10,200 m/s for the exhaust plume constituents. The ambient atmosphere was carried along by the atmospheric wind. The atmospheric wind is a dynamic flow of gas which can travel at

Table 5. Sample of MSIS modeled densities of minor species.[17]

Altitude	NUMBER DENSITIES			
km	He/cm^{-3}	Ar/cm^{-3}	H/cm^{-3}	N/cm^{-3}
320	6.29E+06	7.27E+03	1.31E+05	6.69E+06
322	6.23E+06	6.62E+03	1.31E+05	6.46E+06
324	6.17E+06	6.03E+03	1.30E+05	6.24E+06
326	6.12E+06	5.49E+03	1.30E+05	6.03E+06
328	6.06E+06	5.00E+03	1.30E+05	5.82E+06
330	6.00E+06	4.55E+03	1.30E+05	5.62E+06
332	5.95E+06	4.14E+03	1.29E+05	5.43E+06
334	5.89E+06	3.77E+03	1.29E+05	5.25E+06

**Model is for the date April 26, 2000, hour 19.5 UT, geographical latitude of 31 degrees and geographical longitude of 43 degrees.

velocities from 200 to 900 m/s in the thermosphere and ionosphere.[33] No information is available about the velocity of the atmospheric wind for the time-frame of this experiment. Therefore, an average atmospheric wind velocity of 550 m/s will be used to develop the energy availability values.

6.2.1 Energy Available

The minimum energy produced in the OH reaction of equation 2, by the collision of atomic oxygen (of mass 2.66×10^{-26} kg) with gaseous water (of mass 2.99×10^{-26} kg) from the exhaust plume, is shown in equation 6 to be

$$E_{CM} = \frac{1}{2}\mu(\vec{v}_{[O]} - \vec{v}_{[H_2O]})^2 = 5.07eV \,. \tag{6}$$

Here the reduced mass is given by

$$\mu = (\frac{1}{m_{[O]}} + \frac{1}{m_{[H_2O]}})^{-1} = 1.407 \times 10^{-26} kg \,, \tag{7}$$

and the respective velocities are given by $\vec{v}_{[O]} = 0.55\frac{km}{s}$ and $\vec{v}_{[H_2O]} = 10.2\frac{km}{s}$.

Because the engines were retrofired against the atmospheric wind, these velocities are additive.

The proposed NH reactions, of equation 4 with atomic nitrogen (of mass 2.33×10^{-26} kg), and equation 5 with molecular nitrogen (of mass 4.66×10^{-26} kg), colliding at $\vec{v} = 0.55 \frac{km}{s}$ with the gaseous water produces the average available energies found in equations 8 and 9 respectively.

$$E_{CM} = \frac{1}{2}\mu(\vec{v}_{[N]} - \vec{v}_{[H_2O]})^2 = 4.72eV \quad (8)$$

$$E_{CM} = \frac{1}{2}\mu(\vec{v}_{[N_2]} - \vec{v}_{[H_2O]})^2 = 6.57eV \quad (9)$$

6.2.2 Energy Required to Excite

For these reactions to occur, the colliding molecules must be properly oriented for the product molecule bonds to be formed. Additionally, the collision pair must impact with sufficient energy to overcome the activation energy required for the reaction to proceed.[34] The energy required to proceed begins with the bond dissociation. This is the energy required to break bonds in the reactants and make the constituent atoms available for formation of the products. Following this, the atoms expend bond energy to reassemble into the products. Table 6 summarizes the energies of the reactions being considered.

6.3 Kinetics

In addition to the study of the collision theory of reactions, chemical kinetics is also concerned with the rate of reactions. The rate of a reaction refers to the change in concentration of either the products or reactants over the duration of their interaction. Here a generic mathematical method to calculate the decrease in concentration of the reactant species is outlined. Consideration of values for several variables introduced in this calculation

Table 6. Proposed reactions and their associated energies.[35]

Proposed Reaction	Dissociation Energy	Bond Energy	Available Energy	
			Without Wind	With Wind
O (^{3}P) + H_2O → OH (A $^2\Sigma^+$) + OH (X $^2\Pi$)	4.8 eV	4.05 eV	4.57 eV	5.07 eV
N + H_2O → NH (A $^3\Pi$) + OH (X $^2\Pi$)	4.8 eV	3.69 eV	4.25 eV	4.72 eV
N_2 + H_2O → NH (A $^3\Pi$) + OH (X) + N	11.97 eV	3.69 eV	5.91 eV	6.57 eV

allows the equations to be fully utilized in the next chapter to determine a key characteristic of the reactions generating the radiating OH and NH species.

6.3.1 Chemical Kinetics

The generic formulation of a one-step rate equation begins with the molecular equation for the formation of the emitting species,[36] denoted by C*

$$A + B \xrightarrow{k_1} C^* + D \tag{10}$$

$$C^* \xrightarrow{k_{rad}} C + Q \tag{11}$$

where Q is the number of emissions. The rate of emission is:

$$\frac{dQ}{dt} = k_{rad}\left[C^*\right], \tag{12}$$

where the brackets indicate number density and the rate constant of the radiating reaction is

$$k_{rad} = \frac{1}{\tau_{rad}}. \tag{13}$$

The differential equation for $\left[C^*\right]$ is

$$\frac{d[C^*]}{dt} = -k_1[A][B] - (-k_{rad}[C^*]). \tag{14}$$

where the reaction rate constant has dimensions of $\frac{m^3}{s}$ and may be expressed as

$$k_1 = \frac{1}{[B]\tau_1}. \tag{15}$$

It can be assumed that the time constant, τ_1, of the atmospheric species, denoted by the letter B, is a constant since [B] is not significantly depleted by reactions with A. If the time constant, τ_{rad}, associated with reaction rate constant for the emitting species is much greater than τ_1,

$$\frac{d[C^*]}{dt} = 0 \tag{16}$$

and

$$[C^*] = \frac{k_1}{k_{rad}}[A][B]. \tag{17}$$

The total intensity equation then becomes

$$\frac{dQ}{dt} = k_{rad}\frac{k_1}{k_{rad}}[A][B] = k_1[A][B] = \frac{[A]}{\tau_1}. \tag{18}$$

The differential equation for $[A]$ is

$$\frac{d[A]}{dt} = -k_1[A][B]. \tag{19}$$

Using the Laplace transform equation[37]

$$\mathcal{L}[f'(t)] = s\,\mathcal{L}[f(t)] - f(0), \tag{20}$$

in conjunction with the identity $k = k_1[B]$ and the initial conditions, equation 19 becomes

$$s[A] - (\frac{d[A]}{dt})_0 = -k[A], \tag{21}$$

or,

$$[A] = \frac{(\frac{d[A]}{dt})_0}{s+k}. \tag{22}$$

Taking the inverse Laplace transform of equation 22 gives the concentration of species [A] as

$$[A] = (\frac{d[A]}{dt})_0 \exp(-kt). \tag{23}$$

or, in terms of the time constant,

$$[A] = (\frac{d[A]}{dt})_0 \exp(-\frac{t}{\tau_1}) . \quad (24)$$

Insertion of this value into equation 18 gives

$$\frac{dQ}{dt} = \frac{1}{\tau_1}(\frac{d[A]}{dt})_0 \exp(-\frac{t}{\tau_1}) \quad (25)$$

Integration of this equation over time gives the total radiant intensity resulting from a one-step change in concentration of the species producing the radiation.

$$Q_1 = (\frac{d[A]}{dt})_0 (1 - \exp(-\frac{t}{\tau_1})) \quad (26)$$

Further manipulation along these lines would produce the total radiant intensity equation for a two-step change in concentration as well.[38]

$$Q_2 = (\frac{d[A]}{dt})_0 \{1 - \exp(-\frac{t}{\tau_2}) - \tau_1 [\frac{\exp(-\frac{t}{\tau_1}) - \exp(-\frac{t}{\tau_2})}{\tau_1 - \tau_2}]\} \quad (27)$$

6.3.2 Collision Cross Section

The rate coefficients for the observed collisional excitation processes in this experiment have not been measured. However, the temperature-dependent rate coefficient of the Arrhenius form has been modeled for the hydroxyl reaction.[39] This estimate has proven to lead to an over-prediction of the OH ($A\ ^2\Sigma^+ \rightarrow X\ ^2\Pi$) radiance.[22] Noting the relationship of equation 15, recent efforts on the hydroxyl reaction have turned to determination of the collision cross section.[9]

In the reactant concentration equations above, the one-step time constant is defined as:

$$\tau_1 = (\sigma_1 v_{rel} [B])^{-1} . \quad (28)$$

The sigma term is the total hard-sphere cross section for $A + B$ collisions at the relative atmosphere/plume velocity. The bracketed term is the local density of the atmospheric species. The simplest way to model two colliding molecules

is to assume that they are hard spheres.[40] If they experience an elastic collision, in which the total kinetic energy remains unchanged, the molecules do not react. If the molecules experience an inelastic collision, in which the kinetic energy changes, they may react. To react, the molecules need sufficient energy to overcome the activation threshold energy.

Variable hard-sphere models have been calculated by Kofsky, et al.[41] For the collision partners of gaseous water and atomic oxygen, the inelastic cross section of 6.2 $Å^2$ is proposed. The cross section proposed by Kofsky for the collision partners of molecular nitrogen and gaseous water is 14 $Å^2$. Karabadzhak, in reference 9, proposes a cross section of 20 $Å^2$ for the atomic oxygen and water reaction, but offers no estimates for a molecular nitrogen collision with water. No reference was found which considered the reaction of atomic nitrogen with gaseous water in the exhaust plume.

6.3.3 Model for MirEx data

It must be pointed out that the number density of [A], the plume effluent component, in equation 19 is a dynamic quantity. It is the product of the elapsed time, the mole fraction of the species under examination, a, and the total number of molecules entering the plume per second, N_T, divided by the total volume of the plume at that time

$$[A] = \frac{aN_T t}{V_{t<t_{\max}}}. \qquad (29)$$

The NARJ model provides the values for a and N_T. However, the dynamic quantity in equation 29 is the volume of the plume. To arrive at a solution for equations 26 and 27, a value for $(\frac{d[A]}{dt})_0$ must be found.

As previously stated, the imager had a field of view of 9.8 degrees. This can be visualized as looking at the plume through the narrow end of a cone. This is geometrically portrayed in figure 16, where the paraboloid represents the initial shape of the plume, with the spacecraft engine at the apex. The

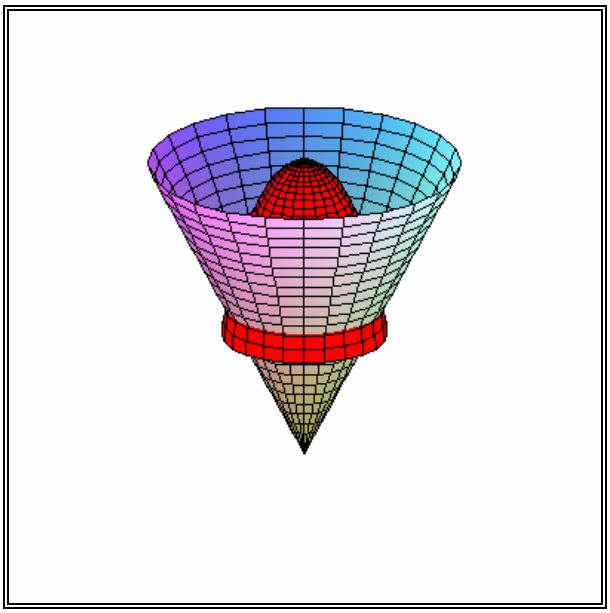

Figure 16. Plume expansion within FOV cone.

height of the cone gives the separation distance between *Mir* and *Progress*, while the cone itself represents the angular FOV encompassed by the imager. At the start of the ACS engines firing the exhaust plume filled just a small portion of that cone. As *Progress* traveled away from *Mir*, the volume of space enclosed by the cone increased uniformly in size. The exhaust plume, on the other hand, expanded non-uniformly.

The telemetry data for *Progress*, including altitude, longitude, latitude, slant range, change in velocity, and change in position, was collected in ten second intervals by *Mir*. From this data, it is known that *Progress* started its ACS engines at a slant range of 28.412 km from the Space Station. Therefore, the imager FOV initially covered a radius of

$$r = (\frac{1}{2})\frac{9.8^\circ}{57.3\frac{^\circ}{rad}}(28412m) = 2430m\,. \tag{30}$$

This formula allowed a conversion to be made from the pixel width of the plume image to a plume radius in meters of the first frame after the ACS engines fired.

Returning to the individual SAF files, the area of the FOV occupied by the plume was measured in pixels. The first two seconds after engine firing began, or 50 frames, were examined. The measured expansion of the plume radius, given in meters, is seen figure 17. From this figure, in the first ½ second of engine firing the plume demonstrates a linear, minimal expansion. However, the plume dramatically expands following this period of slow growth to rapidly exceed the imager FOV radius in approximately 3 seconds.

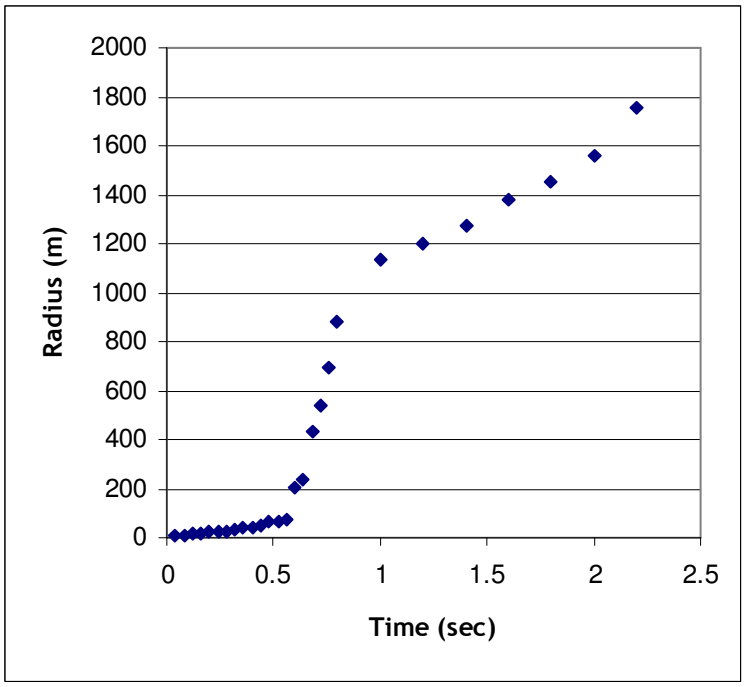

Figure 17. Plume radius expansion.

7 Discussion

Curve fitting can be used with the plume radiant intensity growth and the reaction rate equations to indicate whether the observed chemiluminescent behavior is most likely the result of a one-step or two-step reaction. The utility of the curve fitting method is enhanced by the use of the volume term, which represents the expanding volume of plume effluents within the conical imager FOV.

In this chapter the results of this experiment are discussed. Section 7.1 uses the chemical kinetics equations developed in the last chapter to determine the number of steps in the reaction responsible for forming the excited-state molecules. In Section 7.2, the reactants which meet the energy and reaction step criteria are discussed. Section 7.3 suggests the further utility of the *Progress* data collected on April 26, 2000.

7.1 Intensity Growth of the Progress Plume

Using the value calculated for the initial plume volume, as well as the NARJ modeled plume density, and estimates for the collision cross section, equations 26 and 27 can be solved and plotted. These expected values for radiant intensity give a means for graphical comparison between the chemical kinetics models for one and two-step reactions and the radiance observed by the imager. Cross-frame integration of the radiance from the images during the first seconds after the engines started shows the development of the plume radiant intensity. As is seen in figure 18, the plume intensity development curve (in blue) rises asymptotically from zero to bend over and approach the steady-state radiant intensity, as limited by the imager FOV.

The radiant intensity versus time is strongly dependent on the plume radius expansion, as seen in figure 17. However, for the initial ½ second of engines firing, when the expansion rate is relatively linear and the radius has not grown significantly, the induction behavior of figure 18 is more closely

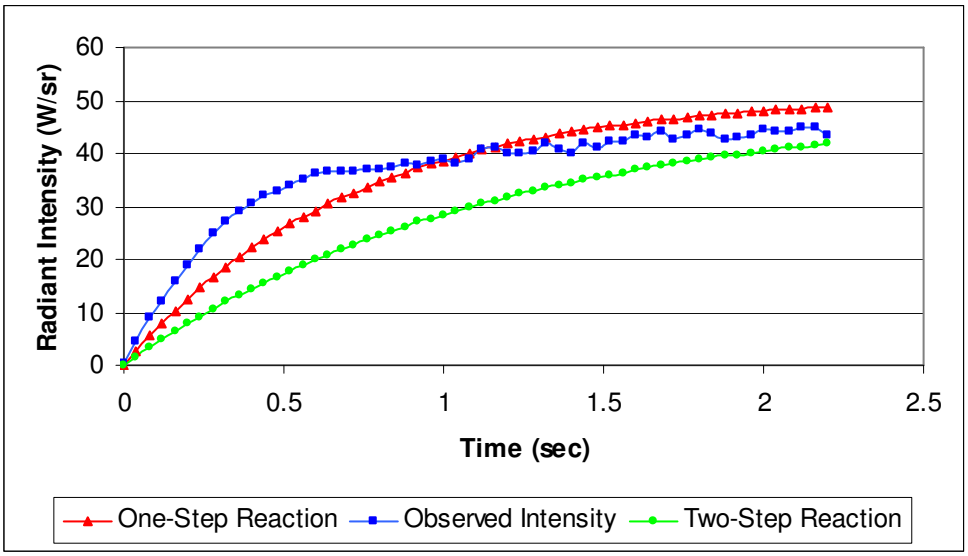

Figure 18. Comparison of plume intensity development.

matched by the one-step reaction model (in red) than the two-step model (in green). It is noteworthy that the theoretical curves representing the reaction models do not include a factor for the atmospheric wind contribution. It is expected that closer agreement with the one-step model will be found when the effect of the wind is included in the model.

The imager observed the wavelengths from 240 nm to 360 nm. Therefore, this induction curve represents the overall behavior in that band-pass region and encompasses both OH and NH bands. If the radiators within the band-pass of the imager were the results of both one and two-step reactions, the resultant plume development curve would be expected to lie between these two regions. Instead, the exponential change in the overall radiant intensity observed as the ACS engines start up more closely resembles the single-step reaction model, albeit with a different time constant.

7.2 Reactants Summary

For unburned fuel fragment collisions with atomic oxygen to be the source of the NH(A), as proposed in equation 3, several reaction steps would be

required. Similarly, as table 6 indicates, there is not enough energy present in the collision of the gaseous water exhaust product with the ambient molecular nitrogen for that reaction to produce the excited-state NH. Therefore, the participation of another atomic ambient atmospheric species with the exhaust plume water is a plausible alternative to the complex molecular collision models. Additionally, at the quantities of atomic nitrogen and oxygen present, as indicated by the MSIS model, there is a large statistical probability of collisions between these species and the spacecraft combustion products.

In the significant literature written on the topic of collisional excitation observed in spacecraft exhaust plumes, the behavior is attributed mainly to multi-step reactions of atomic oxygen with unburned fuel fragments. Simple reactions between atomic species and exhaust effluents have been largely disregarded due to a lack of sufficient activation energy. Furthermore, the contribution of the atmospheric wind has not been considered. The conclusion reached here is that combining the velocity of the atmospheric wind with the exhaust exit velocity in the energy calculations allows consideration of the simple binary reactions of equations 2 and 4 as one-step reaction sources for the excited-state OH and NH molecules.

7.3 Closing Remarks

Other avenues of investigation are possible with this data. Opportunistic data collections by the International Space Station of both Russian spacecraft and US Space Shuttles are on-going. Comparison of the April 2000 data set, along with previous *MirEx* mission data sets, with more recent collections would allow for a wider scope of analysis of Russian spacecraft plumes. Additionally, the differences in engine configurations and fuels used between US and Russian space vehicles are well known. Contrasts in the thermospheric plume characteristics of these vehicles may valuable insight into the operating environment.

Next, further image analysis of the frames during which the first two

narrow-band filters were installed, one with a band-pass of 260 nm and the other with a band-pass of 284 nm, could provide information about processes in a UV region virtually unexploited in the current literature. Finally, the image data includes an observation of the Earth-limb crossing the FOV. This occurrence is also captured in the spectrometer data. While noise is certainly an issue with the spectrometer, the data shows the fascinating ebb and flow of photon saturation going through the wavelength scale. Analysis of the imager and spectrometer data during this event will confirm that, far from being exhausted, much is still to be learned from the *MirEx* data products.

References

References

1.) Drakes, J. A. and Cox, V., *Development of in-situ S&T and T&E Capabilities Aboard the Mir and International Space Stations*, ITEA "T&E and S&T- Forging Partnerships for the Future of Aerospace" conference, Tullahoma, TN, October 12-15, 1999.

2.) Free Software Foundation, *Wikipedia Encyclopedia*, Retrieved 1/1/2006 from http://www.answers.com/topic/mir-1

3.) Harland, D., *Mir and Its Objectives*, Retrieved 1/2/2006 from http://satobs.org/mir.html

4.) Orient, O. J., Chutjian, A., and Murad, E., *Observation of CH A→X, CN B→X and NH A→X Emissions in gas-phase collisions of fast O(^{3}P) Atoms with Hydrazines,* Journal of Chemical Physics, Volume 101, Number 10, November 15, 1994.

5.) Murad, E., *Spacecraft Interaction with Atmospheric Species in Low Earth Orbit,* Journal of Spacecraft and Rockets, Vol. 33, No. 1, January 1996, p. 131-136.

6.) National Aeronautics and Space Administration, **A Russian Space Station: The Mir Complex**, NASA, Houston, TX, February 10, 1994.

7.) Zak, A., *Manned Spaceflight,* Retrieved 8/16/2005 from http://www.russianspaceweb.com/mir.html

8.) Karabadshak, G. F., Khmelinin, B., Plastinin, Y. A., and Rodionov, A. V., *Analysis of New Spacecraft Plume Glow Data Taken Onboard of the Mir Space Station*, "AIAA 41st Aerospace Sciences Meeting & Exhibit", Reno, NV, January 6-9, 2003, AIAA 2003-509.

9.) Anfimov, N. A. and Karabadzhak, G. F., *Studying of Atomic and Molecular Interaction Processes in Rarified Hypervelocity Expanding Flows by Methods of Emissive Spectroscopy,* Final Report for ISTC/EOARD/TSNIIMASH Partner Project #2234p, Feb 2004.

10.) Karabadzhak, G. F., Plastinin, Y. A., Rodionov, V., Erofeev, A. I.,

Freedlander, O. G., *Modeling of the Radiation Caused by Interaction of a Liquid Propellant Motor Exhaust with Rarified Atmosphere at Orbital Altitudes and Comparison with Experiment*, "AIAA 43rd Aerospace Sciences Meeting & Exhibit", Reno, NV, January 10-13, 1999, AIAA 2005-770.

11.) Gimelshein, S. F., Levin, D. A., and Karabadzhak, G. F., *Modeling of Jet Interactions in a Space Environment Using the Direct Simulation Monte Carlo Method*, AIAA 2003-1032.

12.) Zhong, J., Zeifman, M. I., Levin, D. A., and Gimelshein, S. F., *Simulation Monte Carlo Modeling of Homogeneous Condensation in Supersonic Plumes*, AIAA Journal, Volume 43, Number 8, August 2005.

13.) Matsika, S. and Yarkony, D. R., *Conical Intersections and the Nonadiabatic Reactions* $H_2O+O(^3P) \leftarrow\rightarrow OH(A\ ^2\Sigma^+)+OH(X\ ^2\Pi)$, Journal Of Chemical Physics, Volume 117, Number 8, August 22, 2002.

14.) Simmons, F. S., **Rocket Exhaust Plume Phenomenology**, 1st Edition, The Aerospace Press, El Segundo, CA, 2000.

15.) McEwan, M. J. and Phillips, L. F., *Chemistry in the Upper Atmosphere*, Accounts of Chemical Research, Volume 3, Number 1,1970, p. 9-17.

16.) Mueller-Wodarg, I. and Bunce, E., *Comparative Aeronomy in the Solar System*, Astronomy & Geophysics, Volume 44, Issue 2, 2003, page 33.

17.) Levin, D. A., Gimelshein, S. F., Drakes, J. A., Hiers, R. S., Karabadzhak, G. F., and Plastinin, Y. A., *Modeling of Emissions from the Soyuz, Progress, and Mir Rocket Exhaust Plumes at High Altitudes*, AIAA 2000-0601.

18.) National Space Science Data Center, *Atmosphere*, retrieved 4/4/2005 from http://nssdc.gsfc.nasa.gov/space/model/atmos/msise.html

19.) Free Software Foundation, *Wikipedia Encyclopedia*, Retrieved 1/22/2006 from http://en.wikipedia.org/wiki/Space_Elevator_Economics

20.) Karabadzhak, G. F., Plastinin, Y. A., Khmelinin, B., Teslenko, V., Shvets, N., Drakes, J. A., Swann, D. G., and McGregor, W. K.,

Experimentation Using the Mir Station as a Space Laboratory, "AIAA 36th Aerospace Sciences Meeting & Exhibit", Reno, NV, January 12-15, 1998, AIAA 98-0288.

21.) Karabadzhak, G. F., Plastinin, Y. A., Afanasiev, A., Szhenov, E., Drakes, J. A., McGregor, W. K., Nichols, J. A., Reed, R. A., Bradley, D., Teslenko, V., Shvets, N., Volkov, O., and Kukushkin, V., *Measurements of the Progress-M Main Engine Retrofiring Plume at Orbital Conditions*, "AIAA 37th Aerospace Sciences Meeting & Exhibit", Reno, NV, January 11-14, 1999, AIAA 99-1042.

22.) Karabadzhak, G. F., Plastinin, Y. A., Szhenov, E., Afanasiev, A., Drakes, J. A., McGregor, W. K., Bradley, D, Teslenko, V., Shvets, N., Volkov, O., Kukushkin, V., Gimelshein, S. F., and Levin, D. A., *Mir-based Measurements of the Ultraviolet Emissions from Rocket Exhaust Plume Interactions with the Atmosphere at 380-km Altitude*, "AIAA 38th Aerospace Sciences Meeting & Exhibit", Reno, NV, January 11-13, 1999, AIAA 2000-0105.

23.) The Math Works, Inc., **Image Processing Toolbox** *4.2*, Sixth printing, June 2004.

24.) Drakes, J. A., Swann, D. G., Karabadzhak, G. F., and Plastinin, Y., *DSMC Computations of the Progress-M Spacecraft Retrofiring Exhaust Plume*, AIAA 99-0975.

25.) Rodionov, A. V., Plastinin, Y. A., Drakes, J. A., Simmons, M. A., and Hiers III, R. S., *Modeling of Multiphase Alumina-Loaded Jet Flow Fields*, "AIAA 34th Joint Propulsion Conference", Cleveland, OH, July 13-15, 1998, AIAA 98-3462.

26.) McGraw-Hill Education, **Chemistry: Matter and Change**, retrieved 3/25/2005 from http://www.glencoe.com/sec/science/chemistry/mc/pow/chapter14.shtml

27.) Karabadzhak, G. F., Plastinin, Y., Szhenov, E., Afanasiev, A.,

Khmelinin, B., Teslenko, V., Volkov, O., Kukushkin, V., Drakes, J. A., McGregor, W. K., Gimelshein, S. and Levin, D. A., *Preliminary Analysis of Exhaust Plume Radiation during Soyuz-TM Retrofirings*, "AIAA 34th Thermophysics Conference", Denver, CO, June 19-22, 2000, AIAA 2000-2373.

28.) Kotz, J. C., and Treichel, P., **Chemistry and Chemical Reactivity**, Saunders College Publishing, Fort Worth, 1999.

29.) Gardner, J. A., Dressler, R. A., and Salter, R. H., *Methylhydrazine Reactions with O^+ and Other Ions at Hyperthermal Collision Energies,* Journal of Physical Chemistry, 1994, Volume 98, p. 11630-11636.

30.) Viereck, R. A., Murad, E., Knecht, D. J., Pike, C. P., Bernstein, L. S., Elgin, J. B., and Broadfoot, A. L., *The Interaction of the Atmosphere with the Space Shuttle Thruster Plume: The NH(A → X) 336-nm Emission,* Journal of Geophysical Research, Volume 101, 1996, p. 5371-5380.

31.) Catoire, L. and Swihart, M. T., *Thermochemistry of Species Produced from Monomethylhydrazine in Propulsion and Space-Related Applications,* Journal of Propulsion and Power, Volume 18, Number 16, November 2002.

32.) Viereck, R. A., Murad, E., Knecht, D. J., Broadfoot, A. L., Anderson, E., Bernstein, L. S., and Elgin, J. B., *Optical Emissions from the Interaction of Space Shuttle Plumes with the Atmosphere: The NH(A → X) 336-nm Emission,* "AIAA 33rd Aerospace Sciences Meeting & Exhibit", Reno, NV, January 9-12, 1995, AIAA 95-0447.

33.) Rees, D., Smith, R. W., Signernes, F., Henriksen, K, Brandstrom, U., Harris, M., and Maskall, G, *Observations of Thermospheric Neutral Winds Within the Polar Cusp and the Auroral Oval Using a Doppler Imaging System (DIS),* Annales Geophysicae, 1998, Volume 16, p. 1461-1474.

34.) Bernstein, L. S., Chui, Y., Gardner, J. A., Broadfoot, A. L., Lester, M. I.,

Tsiouris, M., Dressler, R. A., and Murad, E., *Molecular Beams in Space: Sources of OH(A→X) Emission in the Space Shuttle Environment*, Journal of Physical Chemistry A, 2003, Volume 107, p. 10695-10705.

35.) Herzberg, G., **Molecular Spectra and Molecular Structure: Spectra of Diatomic Molecules**, 2nd Edition Reprint, Krieger Publishing Company, Malabar, FL, 1989.

36.) Steinfeld, J. I., Francisco, J. S., and Hase, W. L., **Chemical Kinetics and Dynamics,** 2nd Edition, Prentice-Hall, Inc, Upper Saddle River, NJ, 1998.

37.) Arfken, G. B. and Weber, H. J., **Mathematical Methods for Physicists**, 5th Edition, Academic Press, San Diego, CA, 2001.

38.) Dimpfl, W. L., Light, G. C., and Bernstein, L. S., *Molecular Dynamics from Remote Observations of CO(α) from Space Shuttle Plumes,* Journal of Spacecraft and Rockets, Volume 42, Number 2, March 2005.

39.) Cohen, N. and Westberg, K. R., *Chemical Kinetic Data Sheets for High Temperature Chemical Reactions*, Journal of Physical Chemistry Reference Data, Vol. 12, 1983, page 531-558.

40.) Bird, G. A., **Molecular Gas Dynamics**, Clarendon Press, Oxford, 1976.

41.) Kofsky, I. I., Barrett, J. L., Brownrigg, T. E., McNicholl, P. N., Tran, N. H., and Trowbridge, C. A., *Excitation and Diagnostics of Optical Contamination in the Spacecraft Environment,* AFGL-TR-88-0193. July 1988.

Vita

Karen Norton is a native of Bangor, Maine. She graduated from Bangor High School in 1983, and proceeded to work as a commercial radio disc jockey and then as a civil service bookkeeper, before joining the US Navy in 1987. As an Aviation Electronics Technician, she specialized in P-3C infrared and radar systems. Karen deployed onboard both the USS Enterprise (CVN-65) and the USS Harry S. Truman (CVN-75) providing flight deck support of both E-2C Hawkeye and C-2A cargo aircrafts. Additionally, she has seen duty at numerous Navy bases and support sites throughout the world. AT1(AW) Norton was honorably discharged in June 2001, and set out to complete her long neglected higher education. She graduated from the State University of New York, College at Oneonta in May 2004 with a Bachelor of Science degree. There she majored in Physics while earning dual minors in Chemistry and Mathematics. Graduating with honors, she was also a member of Sigma Pi Sigma, the National Physics Honor Society. Karen is currently employed as an Engineer/Scientist by Aerospace Testing Alliance located at the Arnold Engineering Development Center in Tullahoma, Tennessee. She will receive her Master of Science degree in Physics from the University of Tennessee Space Institute in August of 2006.